

Improved constraint on the Hubble constant from dark sirens with LIGO/Virgo/KAGRA O4a

Viviane Alfradique¹,* Clécio R. Bom¹, Gabriel Teixeira¹, and André Santos¹
*Centro Brasileiro de Pesquisas Físicas,
Rua Dr. Xavier Sigaud 150,
22290-180 Rio de Janeiro, RJ, Brazil*

(Dated: March 23, 2026)

A new measurement of the Hubble constant H_0 is presented using the statistical dark siren method applied to a sample of seven well-localized gravitational-wave (GW) events from the fourth LIGO–Virgo–KAGRA (LVK) observing run and ten additional events from the first three runs. Galaxy catalogs from the DESI Legacy Imaging Survey (LS) are combined with a deep learning model to compute photometric redshift probability density functions. We extend our previous analysis by including the events GW230731_215307 and GW230927_153832, using sky maps from the fourth Gravitational-Wave Transient Catalog (GWTC-4), and introducing key methodological improvements: r -band luminosity weighting of host galaxies; an extended GW likelihood that incorporates information from the binary black hole component masses; and a consistent treatment of selection effects that accounts for the incompleteness of the magnitude-limited LS galaxy catalog. Using a total of 17 well-localized dark sirens (seven from the first part of the fourth observing run, O4a), we obtain $H_0 = 78.8^{+14.6}_{-12.2}$ km/s/Mpc without luminosity weighting and $H_0 = 78.2^{+12.0}_{-11.0}$ km/s/Mpc when applying r -band luminosity weighting. Finally, we combine the luminosity-weighted dark siren sample with the bright siren GW170817, including constraints on the jet viewing angle and corrections for the host galaxy peculiar velocity, to obtain a final constraint of $H_0 = 69.9^{+4.1}_{-4.0}$ km/s/Mpc, representing an improvement of approximately 11% in the uncertainty relative to the GW170817-only result.

I. INTRODUCTION

Since its emergence, multimessenger astronomy has transformed both astrophysics and cosmology. The synergy between electromagnetic and gravitational wave observations, and potentially future neutrino detections [1–6], has opened the possibility to investigate phenomena from matter at extreme densities in neutron stars [7–11] to precision measurements of cosmological parameters and tests of general relativity in a strong gravity field regime [6, 12, 13]. Multimessenger observations have already placed constraints on the neutron star equation of state [14–16], improved our understanding of binary properties [9, 17, 18], and contributed to a more comprehensive understanding of the physical processes involved in compact object mergers [8, 19–21].

Over the last decade, we have entered the era of precision cosmology, in which multiple observational probes constrain the parameters of the standard Λ CDM model with unprecedented accuracy. This growing precision has revealed considerable tensions between early- and late-time measurements of cosmological parameters, challenging and putting this model to the test. The most significant of these discrepancies is the so-called “Hubble tension” [22–24]: a persistent 5–6 σ disagreement between the value of the Hubble constant inferred from cosmic microwave background measurements by the Planck collaboration [25] and the local distance-

ladder determinations using Cepheid-calibrated supernovae from the SH0ES collaboration [26]. Additional tensions have also emerged, including 2–3 σ discrepancies [27–30] involving the clustering parameter combination $S_8 \equiv \sigma_8 \sqrt{\Omega_{m0}/0.3}$, where σ_8 is the root mean square of the density contrast in spheres of radius $8 h^{-1}$ Mpc and Ω_{m0} is the local matter density parameter. Furthermore, the DESI DR2 baryon acoustic oscillation measurements show a strong 2.8–4.2 σ preference [31, 32] for a dynamical dark energy component over the Λ CDM model.

In light of these tensions, GWs can serve as an independent cosmological probe, since they provide a direct measurement of the luminosity distance. Combined with the redshift of the host galaxy, they enable the construction of the Hubble diagram. This method, known as the “standard siren” approach [33–35], has become a powerful probe of cosmic expansion $H(z)$, especially since its first multi-messenger validation with GW170817 [36]. That event provided the first direct measurement of H_0 [37] and highlighted standard sirens as a promising tool for clarifying current cosmological tensions. When a merger produces a detectable electromagnetic counterpart, as in GW170817, in which an optical transient and gamma-ray burst enabled identification of the host galaxy NGC 4993 [38–43], the event is referred to as a bright siren.

An alternative way to use GWs to probe $H(z)$ is the statistical dark siren method, in which no electromagnetic counterpart is identified, and the galaxy distribution within the GW localization region is used to estimate the source redshift. Currently, two dark siren techniques have been validated with observational data. The

* vivianeapa@cbpf.com

first, the statistical dark siren method, assumes that each galaxy within the localization region is a potential host and assigns it a probability of hosting the event based on its position [33, 44–54]. The second approach relies on the spatial cross-correlation between the galaxy distribution and the population of GW mergers [55–61]. Additionally, another class of method, using only GW data, aims to break the degeneracy between luminosity distance and redshift by exploiting features of the GW source parameters themselves, such as the intrinsic mass spectrum (the spectral siren method, [53, 62–68]), the spin distribution (spinning spectral sirens, [69]), or, in the case of neutron star binaries, the binary-Love relations, which relate the tidal deformability to the source-frame mass through an EOS-dependent relation (the “Love sirens”, [70, 71]).

In this work, we focus on the statistical dark siren method to obtain a measurement of H_0 , using the latest observations from the LVK O4a run combined with galaxy information from the public LS Survey catalog. We update the results presented in Bom et al. [51] by adding two new dark siren events to the sample and introducing several methodological improvements: (1) applying r -band luminosity weighting to each potential host galaxy; (2) using an extended GW likelihood that accounts for the dependence on BBH component masses; and (3) accounting for the incompleteness of the LS magnitude-limited galaxy catalog in the electromagnetic selection function. The analysis uses the sky maps released in GWTC-4 [72], rather than the initial sky maps released shortly after the GW alerts. Throughout our analysis, we adopt a flat Λ CDM cosmology with a fixed matter density parameter, $\Omega_m = 0.3$, as our fiducial model.

II. DATA

A. LIGO O4a run observation data

In this work, we revisit the five O4a GW events analyzed in [51] (GW230627.015337, GW230919.215712, GW230922.020344, GW231206.233901, and GW231226.101520) and additionally include two new events, GW230927.153832 and GW230731.215307, resulting in a final sample of seven dark standard sirens from the O4a run. These events were selected to focus on well-localized sources, which are expected to provide the most informative posterior on H_0 . The selection criteria adopted were the same as those used in previous works [47, 50, 51]: (1) a luminosity distance $d_L < 1500$ Mpc, (2) a 50% credible sky area $A_{50\%} < 1000$ deg², and (3) at least 70% probability coverage by the LS. The adopted cuts were propagated into the modeling of GW selection effects so that the dark siren H_0 inference remained fully consistent with the applied event selection.

Our selection criteria initially included GW230518.125908 and GW230529.181500. How-

ever, these events were excluded from the analysis. The first was detected during the engineering run (pre-O4) and was removed to avoid potential inconsistencies arising from non-standard detector conditions, which are not accounted for in our modeling of the GW selection effects. The second is consistent with a neutron star–black hole merger and was excluded to ensure consistency with this modeling, developed specifically for BBH events. For all GW events included in our analysis, we used posterior samples generated with the IMRPhenomXPHM_SpinTaylor waveform model, as presented in [73].

The information for our dark siren sample is reported in Table I. The sky coverage of the photometric redshift (photo- z) catalog for each GW event was estimated using the Multi-Order Coverage (MOC) maps defined by the International Virtual Observatory Alliance and implemented through the `mocpy` Python library [74]. MOCs provide a compact representation of arbitrary sky regions based on the hierarchical equal-area pixelization scheme of Hierarchical Equal Area isoLatitude Pixelation of a sphere (HEALPix, [75]). In this framework, sky regions are encoded as sets of HEALPix cells across multiple orders, enabling efficient spatial operations via integer-based set algebra rather than special polygon clipping. To estimate the coverage, we first filtered the LS catalog by converting photo- z into luminosity distances under a fiducial cosmology consistent with the Planck 2015 constraints [76]. Galaxies within the luminosity distance range compatible with each GW event were retained as potential hosts. We then constructed an MOC representation of the spatial distribution of the selected galaxies using their sky coordinates. The MOC was generated at a maximum HEALPix order of 11, corresponding to an angular resolution of approximately 1.7 arcminutes. At this order, each retained galaxy contributes its enclosing HEALPix cell, effectively approximating the angular footprint of the photo- z catalog at the chosen resolution. Independently, the GW sky map was converted into a MOC by selecting HEALPix pixels comprising the 90% CI, determined by ranking pixels in descending probability density and integrating until the cumulative probability reached 0.9. This region was likewise represented at maximum order 11 to ensure consistent angular resolution between datasets. The fractional photo- z coverage of the GW localization area was computed by intersecting the galaxy MOC with the 90% CI GW MOC. The sky area of the intersection ($\Omega_{\text{photo-}z \cap \text{GW}, 90\%}$) and the area corresponding to the full GW credible region ($\Omega_{\text{GW}, 90\%}$) were calculated directly from the solid angles of their constituent HEALPix cells using `mocpy`. The coverage fraction is therefore defined as

$$f_{\text{cov}} = \frac{\Omega_{\text{photo-}z \cap \text{GW}, 90\%}}{\Omega_{\text{GW}, 90\%}}, \quad (1)$$

where the sky areas (in steradians) are derived from the MOC representations. This procedure ensures that the coverage estimate is resolution-controlled, computation-

ally efficient, and fully consistent with the probabilistic structure of the GW localization. Three events have less than 90% coverage of their credible regions, with two of them lying exactly at the threshold of our adopted selection criterion. For these events, we injected fake galaxies (following the same procedure used in our previous work, Bom et al. 51; see the description in Section III B) into the uncovered regions to reproduce the completeness correction commonly applied in dark siren analyses [46, 73, 77–79]. In the last column of Table I, we present the number of galaxies within the GW sky localization. The number inside the parentheses corresponds to the number of galaxies remaining after applying the apparent magnitude (survey sensitivity) cut, the absolute magnitude cut (to ensure a volume-limited sample, as detailed in the next subsection), and the additional quality cuts described in the following subsections. The number outside the parentheses indicates the total number of galaxies before any cuts are applied.

B. DESI Legacy Survey data

The DESI Legacy Imaging Survey [80] is a combination of three public imaging surveys: the Dark Energy Camera Legacy Survey [81], the Beijing-Arizona Sky Survey [82], and the Mayall z -band Legacy Survey [83]. Together, these surveys image a large fraction of the extragalactic sky. Imaging of the southern and equatorial regions was carried out with the Dark Energy Camera (DECam [84]) as part of the DECam Legacy Survey (DECaLS), while the northern footprint, at declinations $\delta \gtrsim +32^\circ$, was imaged in gr obtained with the Bok 2.3-m telescope as part of the Beijing-Arizona Sky Survey (BASS), and z -band imaging acquired with the Mosaic-3 camera on the Mayall 4-m telescope as part of the Mayall z -band Legacy Survey (MzLS). The photometric coverage was extended to include the i -band via additional DECam observations, with most of the data originating from the full six years of Dark Energy Survey [85], the DECam Local Volume Exploration Survey (DELVE [86]), and the DECam eROSITA Survey (DeROSITAS [87]). The imaging reaches typical 5σ point-source depths of $g \sim 24.0$, $r \sim 23.4$, $z \sim 22.5$ AB mag. In this work, we primarily use the publicly available catalog from Data Release 10 (LS-DR10 [88]), which spans approximately $20,000 \text{ deg}^2$. For regions in the northern footprint, we instead use Data Release 9 (LS-DR9 [89]), which includes imaging from the BASS and the MzLS that are not included in DR10. To estimate the catalog completeness, we show that the LS r -band absolute magnitude distribution is well described by a Schechter function adopting the SDSS-derived parameters [90], $M_{*,r} = -20.44$, $\alpha = -1.05$, and $\phi_* = 1.49 \times 10^{-2} h^3 \text{ Mpc}^{-3}$. Figure 1 illustrates this behavior, showing good agreement at the bright end and the expected decline toward the survey threshold. Given this luminosity function and the adopted r -band survey depth, we find that the LS achieves $\sim 99\%$ completeness

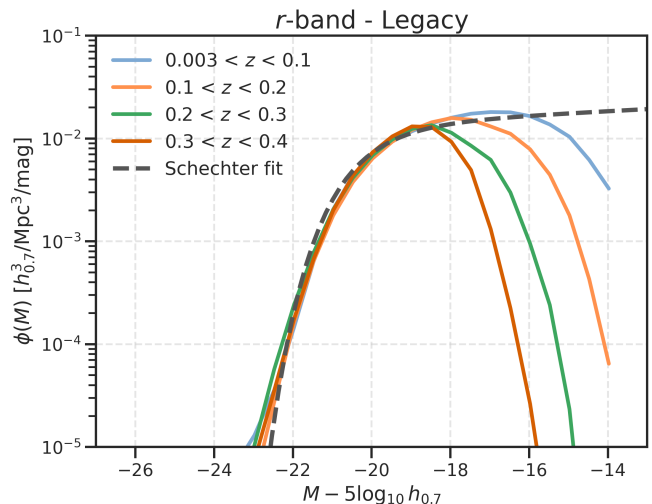


FIG. 1. Schechter-function fit (gray) to the galaxy luminosity distributions of the LS in the r -band. Different colors correspond to different redshift bins.

at $z = 0.5$ for $M_r < -18.09$, and $\sim 98\%$ at $z = 0.6$ for $M_r < -18.56$.

To ensure that the resulting catalog is volume-limited, we follow the procedure described in previous work [47, 50, 51, 91]. First, for each dark siren event, we compute the maximum redshift corresponding to the upper limit of the 90% CI on the luminosity distance, adopting the highest value of our H_0 prior. Given the apparent magnitude threshold at this maximum redshift, we then compute the faintest absolute magnitude that a galaxy could have and still satisfy the survey magnitude limit. All galaxies in the catalog with absolute magnitudes fainter than this threshold are removed. Throughout this procedure, we assume our fiducial Λ CDM cosmology.

C. Photometric redshift estimation with Mixture Density Networks

The photometric redshifts used in this work were estimated using a deep learning model following the methodology presented in Bom et al. [51]. This method is based on mixture density networks (MDNs, [92]), a technique that estimates probability density functions (PDFs) for the redshifts, represented as a mixture of Gaussians.

For galaxies with declination below 30 deg , we adopt the publicly available photometric data from the LS-DR10. For this subsample, we directly used the same MDN model presented in Bom et al. [51], ensuring that our photo- z estimates achieve the same level of performance reported in that work.

In contrast, for galaxies with declination above 30 deg , we adopt a different strategy using LS-DR9 data. Instead of using a model trained on the combined northern and southern samples, as in Bom et al. [51], we train the

TABLE I. Summary of the properties of the O4a dark siren events analyzed in this work. Columns list, in order: the GW event name; the primary and secondary BH masses; the luminosity distance; the 90% credible interval (CI) sky area and volume; the false alarm rate; the sky map coverage (in percent); and the number of potential host galaxies ($N_{\text{gal,host}}$). The measurements are derived from posterior samples generated with the IMRPhenomXPHM_SpinTaylor waveform model, as provided by LIGO Scientific Collaboration [73], while the sky map coverage and $N_{\text{gal,host}}$ are computed as described in the text.

O4a GW event	$m_1^{\text{det}} [M_{\odot}]$	$m_2^{\text{det}} [M_{\odot}]$	d_L [Mpc]	A [deg ²]	V [Gpc ³]	FAR [yr ⁻¹]	Sky map Coverage [%]	$N_{\text{gal,host}}$
GW230627_015337	$9.0^{+1.9}_{-1.3}$	$6.0^{+1.0}_{-0.9}$	307^{+62}_{-131}	92	3.3×10^{-4}	$< 1.0 \times 10^{-5}$	90	3103868(16076)
GW230731_215307	$12.0^{+3.0}_{-1.4}$	$10.0^{+1.2}_{-1.9}$	1113^{+335}_{-453}	629	8×10^{-2}	$< 1.0 \times 10^{-5}$	73	17640655(26348)
GW230919_215712	34^{+7}_{-4}	27^{+3}_{-5}	1275^{+734}_{-483}	570	1.7×10^{-1}	$< 1.0 \times 10^{-5}$	70	17290478(27576)
GW230922_020344	53^{+12}_{-9}	37^{+7}_{-8}	1453^{+763}_{-609}	270	1×10^{-1}	3.6×10^{-4}	98	9032150(5251)
GW230927_153832	27^{+4}_{-3}	$20^{+2.8}_{-2.7}$	1168^{+385}_{-516}	273	4×10^{-2}	$< 1.0 \times 10^{-5}$	70	6235681(5880)
GW231206_233901	48^{+9}_{-5}	37^{+6}_{-8}	1483^{+333}_{-492}	292	6×10^{-2}	1.6×10^{-5}	99	10899526(19288)
GW231226_101520	49^{+7}_{-3}	43^{+3}_{-6}	1168^{+222}_{-301}	136	1×10^{-2}	$< 1.0 \times 10^{-5}$	98	4755915(11367)

MDN using objects exclusively from the northern region of the LS DR9 catalog. The training sample was constructed by first selecting sources with `TYPE` \neq `PSF`, to exclude objects classified as point sources by the LS detection pipeline [80]. We then restrict the sample to objects with available spectroscopic redshift measurements in the same catalog.

To ensure data quality, we excluded objects close to the detection limit by imposing $r < 22.5$, and removed sources with unphysical colors by requiring $-1 < g - r < 4$. These cuts are adapted from those used in Bom et al. [51], although only a subset of their selection criteria was applied here—mostly due to the lack of *i*-band measurements for the northern galaxies. The remaining dataset was randomly split, reserving 20% for testing in order to evaluate the performance of the network after training. Unlike the approach adopted in Alfradique et al. [50], Bom et al. [51], Teixeira et al. [93], we did not homogenize the training distribution due to the limited number of reliable sources (approximately 40,000 objects).

One of the main differences compared to Bom et al. [51] lies in the network architecture. Given the limited size of the training sample, we find that a simpler architecture yields better performance. The model consists of three fully connected layers with 16, 12, and 8 units, respectively, followed by an MDN layer with six Gaussian components.

Figure 2 presents the performance of the new photometric redshifts as a function of *r*-band magnitude, compared to the publicly available estimates. The new model achieves comparable performance in terms of the photo-*z* bias (the averaged $\Delta z = z_{\text{photo}} - z_{\text{spec}}$), defined as the difference between the photometric redshift point estimate and the spectroscopic redshift of the same galaxy, and the outlier fraction (i.e., objects with $\Delta z / (1 + z_{\text{spec}}) > 0.15$), with a slightly larger normalized median absolute deviation ($\sigma_{\text{NMAD}} = 1.48 \times \text{median} [|\Delta z - \text{median}(\Delta z)| / (1 + z_{\text{spec}})]$). Moreover, as shown in Alfradique et al. [50], the use of full photo-*z* PDFs increases the reliability of posterior estimates, making the new LS-DR9-north redshifts particularly well

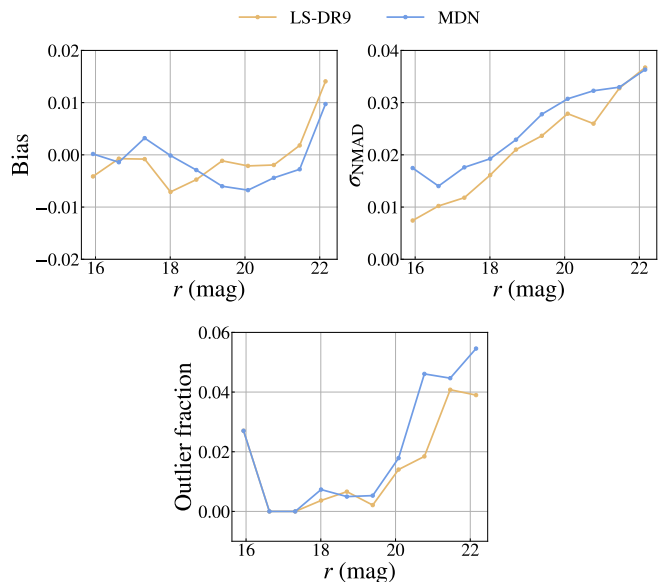


FIG. 2. Performance of the photometric redshift estimates as a function of *r*-band magnitude. We compare the publicly available LS DR9 redshifts with those obtained using the MDN. The panels show the photo-*z* bias, σ_{NMAD} , and outlier fraction.

suit for this application. Further details on the development of these photometric redshifts, as well as the full catalogs, will be presented in Teixeira et al. [94].

III. METHOD

The statistical dark siren method assumes that every bright galaxy within the GW localization volume is a potential host of the event, each assigned a probability of being the true host based on its position. By combining the redshift information from a galaxy catalog with the luminosity distance measurement inferred from the GW signal, one obtains an individual contribution to the posterior on H_0 from each possible host. The final H_0 con-

straint is then obtained by marginalizing over all galaxies in the localization volume. This approach was first proposed by Schutz [33], and Del Pozzo [44] was the first to apply it to simulated data. Later refinements of the method, including additional challenges associated with real data, are described in Chen et al. [77]. In this work, we follow the statistical formulation presented in Chen et al. [77], with modifications introduced in later studies [45, 47, 51, 91].

In the statistical dark siren scenario, we exploit the fact that GW data provide measurements of the luminosity distance, \hat{d}_L , and the GW source solid angle, $\hat{\Omega}_{\text{GW}}$. In contrast, EM data provide measurements of galaxy redshift \hat{z}_i , solid angle $\hat{\Omega}_i$, and apparent magnitude \hat{m}_i for each potential host galaxy i . In this work, we denote measured quantities with a hat and their corresponding true values without.

The joint likelihood of the electromagnetic observations from the galaxy catalog and the GW data can be expressed as the product of two individual likelihoods, $p(d_{\text{GW}}, d_{\text{EM}} | H_0) = p(d_{\text{GW}} | H_0) p(d_{\text{EM}} | H_0)$, since the measurements are independent, where $p(d_{\text{GW}} | H_0)$ and $p(d_{\text{EM}} | H_0)$ denote the GW and EM likelihoods, respectively. In the following, we construct this joint likelihood based on two assumptions: (i) the GW source is hosted by one of the galaxies in the catalog, and (ii) BBH mergers are expected to occur preferentially in more luminous galaxies, as luminosity in specific bands correlates with galaxy properties such as stellar mass and star formation rate. This second assumption is supported by results from synthetic simulations of compact binary mergers, which demonstrate a strong correlation between stellar mass, star formation rate, and the merger rate per galaxy in the local Universe [95–99]. The GW likelihood $p(d_{\text{GW}} | H_0)$ is first marginalized over the true luminosity distance, sky location of the source, and other intrinsic parameters of the GW source (such as spins, masses, and inclination angle). We then marginalize the joint likelihood over the true redshifts, sky positions, and apparent magnitudes of all N_{gal} galaxies in the catalog, such that the joint likelihood can be written as [77]:

$$p(d_{\text{EM}}, d_{\text{GW}} | H_0) \propto \frac{1}{\beta(H_0)} \sum_{i=1}^{N_{\text{gal}}} \int w_i(m_i, z_i) \times p(d_{\text{GW}} | d_L(z_i, H_0), \Omega_i) \prod_{j=1}^{N_{\text{gal}}} p(d_{\text{EM},j} | z_j, \Omega_j, m_j) \times \frac{\psi(z_j) r^2(z_j, H_0)}{(1+z_j) H(z_j, H_0)} dz_j d\Omega_j dm_j, \quad (2)$$

where

$$w_i(m_i, z_i) = \left| \frac{L_i}{L_*} \right| = 10^{-0.4(M_i(m_i, z_i, H_0) - M_*(H_0))} \quad (3)$$

denotes the statistical weight assigned to each galaxy representing the probability that it hosts the GW source,

L_* and M_* are the “knee” luminosity and corresponding magnitude of the Schechter function, $\beta(H_0)$ is a normalization term that ensures the likelihood integrates to unity over all detectable GW and EM datasets, r is the comoving distance, and $H(z, H_0) = H(z, H_0; \Omega_m^{\text{fid}} = 0.3) = H_0 \left(0.3(1+z)^3 + 0.7 \right)^{1/2}$ represents the Hubble parameter in a fiducial flat Λ CDM cosmology. The last term in eq. (2) represents the joint prior on the population-level parameters, defined as the product over all galaxies of their individual redshift priors. We assume that galaxies are uniformly distributed in comoving volume, with a merger rate evolution $\psi(z)$ following the Madau–Dickinson cosmic star formation rate [100]. The factor $(1+z_j)^{-1}$ accounts for the conversion from the source frame to the detector frame.

The statistical weight is based on the second assumption discussed above. As noted by Gray et al. [48], Abac and et al. [52], although the transformation from absolute to apparent magnitude depends on cosmology through the relation $M_i(m_i, z_i, H_0) = m_i - 5 \log_{10}(d_L(z_i, H_0)/\text{Mpc}) - 25 - K_{\text{corr}}(z_i)$, the weights w_i do not depend on H_0 since this dependence is eliminated in the ratio L/L_* , given that L_* follows the same scaling with H_0 . K_{corr} is the K-correction term, which corrects for the shift of a galaxy’s observed spectrum due to redshift, converting the observed magnitude into the equivalent rest-frame magnitude. This term was computed according to Kochanek et al. [101]. We choose to use the galaxy r -band luminosity for weighting, as it most closely corresponds to the near-infrared K -band, which is believed to serve as a reliable proxy for stellar mass [102–104].

Assuming that the observed EM quantities are conditionally independent given the true values, the EM likelihood for the j -th galaxy can be written as

$$p(d_{\text{EM},j} | z_j, \Omega_j, m_j) = p(\hat{\Omega}_j | \Omega_j) p(\hat{z}_j | z_j) p(\hat{m}_j | m_j). \quad (4)$$

The galaxy positions are assumed to be perfectly measured and are represented by Dirac delta functions centered on the observed values. We model the likelihood of the apparent magnitude m_j with a Gaussian distribution, \mathcal{N} , centered on the measured value \hat{m}_j with standard deviation σ_{m_j} .

Following Singer and Price [105], the marginal GW likelihood for the set of source parameters $\{z, \Omega\}$ can be approximated by a Gaussian function, expressed as

$$p(d_{\text{GW}} | d_L(z, H_0), \Omega_i) \propto \frac{p(\Omega_i)}{\sqrt{2\pi}\sigma_{d_L}(\Omega_i)} \times \exp \left[-\frac{(d_L(z, H_0) - \hat{d}_L(\Omega_i))^2}{2\sigma_{d_L}^2(\Omega_i)} \right], \quad (5)$$

where $p(\Omega_i)$ represents the sky position probability, and $\hat{d}_L(\Omega_i)$ and $\sigma_{d_L}(\Omega_i)$ correspond to the mean and standard deviation of the luminosity distance, respectively.

The area of the i -th HEALPix pixel on the sky is defined by Ω_i .

The marginal GW likelihood as defined in eq. 5 accounts only for a subset of the source parameters, $\vec{\theta} = \{z, \Omega\}$. This is based on the assumption that the remaining parameters of the GW waveform are sampled from a population distribution identical to the prior employed in the inference of individual detections. However, as detector sensitivity improves, leading to more precise measurements, and given our limited knowledge of the true population prior for the source-frame masses, this assumption may no longer hold. In such cases, it becomes necessary to explicitly model or marginalize over the possible discrepancies between the assumed and true mass distributions. To account for this, following Gray et al. [48], Abac and et al. [52], Borghi et al. [64], Gray et al. [79] (see equation 18 of Borghi et al. [64]), we approximate the marginal GW likelihood (hereafter referred to as full) using a three-dimensional kernel density estimate (KDE), where the GW posterior, $p(z, m_1, m_2, \Omega | d_{\text{GW}})$, samples are re-weighted by the source-frame prior and the Jacobian of the source-to-detector frame transformation ($|d\vec{\theta}^{\text{det}}(\vec{\theta}, H_0) / d\vec{\theta}|$), as given by:

$$p(d_{\text{GW}} | d_L(z, H_0), \Omega) = \int dm_1 dm_2 \frac{p(z, m_1, m_2, \Omega | d_{\text{GW}})}{p(m_1) p(m_2) p(d_L)} \times \left(\frac{dd_L}{dz}(z, H_0) \right)^{-1} p(m_1, m_2 | \vec{\lambda}_m), \quad (6)$$

where the term $\frac{dd_L}{dz}(z, H_0) = \frac{d_L(z, H_0)}{1+z} + \frac{c(1+z)}{H(z, H_0)}$ is the Jacobian of the transformation from z to d_L , and $p(m_1, m_2 | \vec{\lambda}_m)$ is denotes the BBH mass population model characterized by the parameter set $\vec{\lambda}_m$. The priors and GW posteriors were taken from the results of Abac and et al. [72]. In this work, we adopt the BBH Broken Power Law + 2 Peaks model [106], using the best-fit curve reported by the GWTC-4 population analysis [107].

Substituting the definition of the marginal EM likelihood (eq. 4) into the joint likelihood (eq. 2) and factorizing the product, the joint likelihood can be rewritten and simplified, yielding the posterior for H_0 as:

$$p(H_0 | d_{\text{GW}}, d_{\text{EM}}) \propto \frac{p(H_0)}{\beta(H_0)} \sum_{i=1}^{N_{\text{gal}}} \frac{1}{\mathcal{Z}_i} \int dz_i \int d\Delta z p(\Delta z) \times p(d_{\text{GW}} | d_L(z_i, H_0), \hat{\Omega}_i) p(\hat{z}_i | z_i, \Delta z) \frac{\psi(z_i) r^2(z_i, H_0)}{(1+z_i) H(z_i, H_0)} \times \left(\int_{m_{\text{min}}}^{m_{\text{max}}} dm_i 10^{-0.4(M_i(m_i, z_i, H_0) - M_*(H_0))} \mathcal{N}(\hat{m}_i | m_i) \right), \quad (7)$$

where

$$\mathcal{Z}_i = \int dz_i p(\hat{z}_i | z_i) \frac{\psi(z_i) r^2(z_i, H_0)}{(1+z_i) H(z_i, H_0)} \quad (8)$$

is the evidence terms that correctly normalize the posterior, and $p(H_0)$ is the prior on H_0 , which we assume

to be uniform over the range [20, 140] km/s/Mpc. The integration over apparent magnitude is constrained by two limits: a bright-end cutoff defined by the r -band Schechter function, $M_{\text{min}}(z_{\text{min}}, m_{\text{min}})$, evaluated at the minimum redshift of our galaxy sample, assuming a cosmology with the largest H_0 value from our prior; and a faint-end limit corresponding to the apparent magnitude threshold that characterizes the completeness limit of the galaxy catalog. For the LS, we adopt $m_{r, \text{thr}} = 21$ for this threshold. As shown in Fig. 1, the r -band absolute magnitude distribution of LS galaxies is well described by a Schechter function with parameter values consistent with those reported by Blanton et al. [90]. We therefore adopt the corresponding r -band Schechter parameters: $M_* = -20.44$ and $M_{\text{min}} = -24.26$. In the equation above, the marginal EM likelihood for a given galaxy reduces to $p(\hat{m}_i | m_i) p(\hat{z}_i | z_i) = \mathcal{N}(\hat{m}_i | m_i) p(\hat{z}_i | z_i)$, where $\mathcal{N}(\hat{m}_i | m_i)$ denotes the Gaussian likelihood for the apparent magnitude measurement, and $p(\hat{z}_i | z_i)$ represents the photometric redshift likelihood computed as described in Section II C. We also include a correction for the bias in photo- z , Δz , present in the data. This bias arises because the distribution of galaxies in redshift or color is not uniform beyond certain magnitude or color selection limits, causing the deep learning algorithm to preferentially sample redshifts near the peaks of the distribution and thus introducing systematic errors.

To account for selection effects in the dark siren analysis, we adopt the same definition presented in Fishbach et al. [46], Chen et al. [77], Mandel et al. [108], Gray et al. [109]. This effect is incorporated into a normalization factor that accounts for the biases introduced by the limited sensitivity of both the GW detectors and the survey telescopes, which allows them to observe only a fraction of the total population of compact binary coalescences and their potential host galaxies. Neglecting this correction could introduce significant biases in the inference of cosmological parameters, as discussed in Mandel et al. [108]. Under the assumption that GW events are uniformly distributed across the sky on cosmological scales, the normalization factor, $\beta(H_0)$, can be expressed in a compact form as (see [77, 108]):

$$\beta(H_0) = \int_0^{z_{\text{max}}} p_{\text{sel}}^{\text{GW}}(d_L(z, H_0)) p_{\text{sel}}^{\text{EM}}(d_L(z, H_0)) p(z) dz, \quad (9)$$

where $p(z)$ represents the prior redshift distribution of the galaxy catalog, $p_{\text{sel}}^{\text{GW}}$ represents the probability that a GW event at luminosity distance d_L is detected by the network of detectors, and $p_{\text{sel}}^{\text{EM}}$ is the probability that a galaxy at d_L is observed in the galaxy survey. We assume that the galaxy distribution is uniform in comoving volume, while accounting for the Madau–Dickinson phenomenological model for the star formation rate [100]. The dependence on sky position in the equation above is neglected under the assumption that the sources are isotropically distributed. As pointed out by Palmese et al. [47], Chen et al. [77], the galaxy distribution is not expected to be strongly correlated with the GW detector

antenna pattern; hence, this assumption is not expected to introduce any significant systematic biases.

The term $p_{\text{sel}}^{\text{GW}}$ must include our selection criteria for the well-localized dark siren sample used in this analysis: $A_{50\%} < 1000 \text{ deg}^2$, $d_L < 1500 \text{ Mpc}$, and GW events with more than 70% of their sky localization probability covered by the LS. However, because we do not expect the LS footprint to be correlated with the GW antenna pattern, this last condition does not need to be explicitly included in the computation. In practice, this is equivalent to performing an isotropic random sampling of the GW events. On the other hand, the term $p_{\text{sel}}^{\text{EM}}$ essentially describes the coverage of a given magnitude-limited catalog, as the EM likelihood is considered uninformative in the dark siren context, since no counterpart can be identified and associated with the GW source. The functions $p_{\text{sel}}^{\text{GW}}$ and $p_{\text{sel}}^{\text{EM}}$ are smooth and range from 0 to 1 as a function of redshift, for different assumed values of H_0 .

A. Gravitational wave and electromagnetic selection functions

To model the selection function, we adopted an approach consistent with previous dark siren analyses [47, 50, 51]. In our implementation, we generated a synthetic catalog of 100,000 BBH merger events using the BAYESTAR software [102, 105, 110], employing the IMR-PhenomD waveform model in the frequency domain. The BBH population was drawn from a Broken Power Law + Two Peaks mass distribution, using the best-fit curve reported in Abac et al. [107], and assuming uniform spin distributions in the range $(-1, 1)$. The BBH population was distributed uniformly in comoving volume, assuming the Madau–Dickinson parametrization to describe the redshift evolution of the merger rate. As in the O4a observing run, Virgo and KAGRA were in the commissioning phase (with KAGRA operating for only one month); therefore, the matched-filter analysis used to compute the signal-to-noise ratio (SNR) for each injected event was performed using only the LIGO Hanford and Livingston detectors. The analysis employed the power spectral density estimates provided in LIGO Scientific Collaboration [111] and described in Essick et al. [112]. We adopted a detection criterion requiring a network SNR greater than 12 and an individual detector SNR greater than 4. To mimic realistic measurements, Gaussian noise was added to all injected GW signals. For each detected event, we used BAYESTAR to reconstruct the sky map, assuming a luminosity distance prior proportional to d_L^2 . We performed 25 independent GW simulations, each assuming a different H_0 value within our prior range. The resulting function was interpolated to guarantee a continuous definition over the entire H_0 range.

In the dark siren methodology, the electromagnetic data correspond to the identification of potential host galaxies, in contrast to the bright siren case, where the

electromagnetic counterpart arises from the transient flare produced at the time of the merger, enabling a direct host identification. In this context, the term $p_{\text{sel}}^{\text{EM}}$ accounts for the incompleteness of the magnitude-limited galaxy catalog, in contrast to the bright siren case, where it instead represents the probability of detecting an electromagnetic counterpart and must be modeled accordingly to avoid potential systematics related to EM selection effects and their possible mitigation strategies (see discussions in [113–117]). Here, we compute the galaxy catalog incompleteness for the LS following the procedure of Abac et al. [52]. As established in the previous subsection, the r -band absolute magnitude distribution is well described by a Schechter function with parameter values derived from the SDSS catalog (see Fig. 1). We then adopt the incompleteness definition given in Appendix B2 of Abac et al. [52] (their eq. B20) to evaluate the completeness fraction as a function of z and H_0 for an apparent magnitude threshold of $m_{r,\text{thr}} = 21$. The resulting completeness curves are shown as dashed lines in the top panel of Fig. 3. In the bottom panel, we present two versions of the selection function: (1) considering only the GW detection probability and assuming a Heaviside step function for $p_{\text{sel}}^{\text{EM}}$ at the redshifts of interest (black line), and (2) including the incompleteness of the magnitude-limited galaxy catalog in $p_{\text{sel}}^{\text{EM}}$ (gray line). The two curves differ only slightly, with the relative difference remaining at the percent level across the entire H_0 prior range.

B. Galaxy fakes

The lack of galaxies in the catalog, caused by the sensitivity limitations of optical telescopes, can introduce incompleteness effects, which typically bias the sample toward the bright end of the luminosity distribution and lead to a bias toward a lower H_0 value (as discussed in Alfradique et al. [118]). To correct this effect, it was suggested that the missing galaxies be assumed to be uniformly distributed in comoving volume [46, 49, 64, 73, 77, 109, 119, 120]. However, other studies have noted that assuming uniform completeness introduces biases in the H_0 estimation in the regime where the out-of-catalog term dominates, and have proposed extensions that account for inhomogeneities in the galaxy distribution along the line of sight [78, 79]. Following this approach, Leyde et al. [121] recently proposed a method that reconstructs the missing galaxy distribution by assuming that this field follows the two-point statistics. As shown by Alfradique et al. [118] using simulated detections for the O4 and O5 observing runs, it is possible to obtain an unbiased estimate of H_0 with a volume-limited catalog. Based on this result, and following the approach adopted in previous works (and described in Section II B), we construct our galaxy catalog to be volume-limited and therefore do not include an additional correction term in the dark siren methodology.

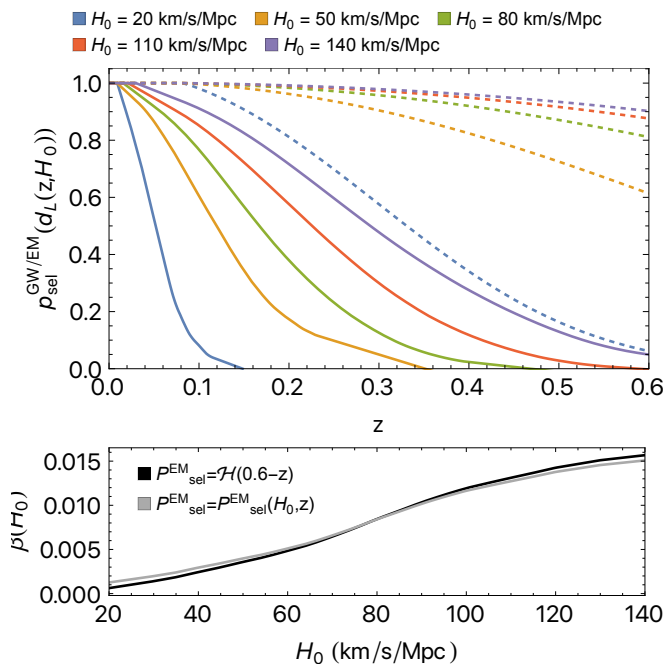


FIG. 3. GW and EM selection functions. **Top panel:** gravitational wave (solid lines) and electromagnetic (dashed lines) detection probabilities as functions of H_0 (shown in different colors) computed for an apparent magnitude threshold of $m_{r,\text{thr}} = 21$. **Bottom panel:** Selection function (as defined in eq. 9) computed from GW detection simulations using BAYESTAR. The black curve shows the result including only the GW detection probability (solid lines in the top panel), while the gray curve includes the EM detection probability as well (dashed lines in the top panel).

Additionally, we inject synthetic galaxies into the regions not covered by the photo- z catalogs to mitigate residual incompleteness. Among our dark siren sample, three GW events (GW230919_215307, GW230927_153832, and GW230731_215307) have 90% CI areas that approach our selection threshold of 70% coverage by the LS catalog.

To mitigate the impact of these uncovered regions, we adopt the procedure described in Palmese et al. [47], Bom et al. [51] to inject synthetic galaxies into the missing areas. The synthetic galaxies are assigned redshifts sampled from the prior defined by the training sample using a Monte Carlo procedure, while their positions are uniformly distributed across the sky with a number density set by the mean density of the LS galaxy catalog. To assign uncertainties in photo- z and apparent magnitude, we first use our training sample to compute the mean and standard deviation within photo- z bins of width 0.05, and then derive the relation between photo- z error or apparent magnitude and photo- z . We assume that the photo- z PDFs of the synthetic galaxies are Gaussian, sampling each value around its assigned true redshift with a standard deviation set by the corresponding photo- z uncertainty. In section IV, we discuss the impact of these synthetic galaxies on our final H_0 constraint.

IV. RESULTS AND DISCUSSION

In this section, we report our estimates of the Hubble constant obtained from the seven O4a gravitational wave events using the statistical dark siren framework introduced in Section III. The analysis combines GW data with photometric redshift probability distributions from the LS, constructed with the deep-learning approach developed in our previous work [50, 51, 93] and described in Section II C. Our results are presented both for individual events and for their joint combination. We focus primarily on two methodological effects in the analysis: (i) the inclusion of r -band luminosity weighting, and (ii) two different implementations of the GW likelihood. These are: (1) a Gaussian approximation that depends only on the source parameters $\{d_L, \Omega\}$, as defined in eq. (5); and (2) the full likelihood obtained from a KDE of the posterior samples, reweighted by the population prior on the source-frame masses, as in eq. (6). In addition, we explore the impact of electromagnetic selection effects and of using photo- z PDFs obtained with the MDN compared to a Gaussian photo- z approximation (see the discussion in App.A).

Figure 4 shows the individual H_0 posteriors for the seven O4a GW events analyzed in this work. The most informative event is GW231206_233901, and its 1σ constraint reaches close to 77% (74%) of the H_0 prior in the unweighted (r -band weighted) case using the full GW likelihood. In contrast, GW230731_215307 and GW230919_215712 yield the weakest constraints: GW230731_215307 leaves 85%(82%) of the prior width, and GW230919_215712 leaves 89%(91%) in the same configurations. These events are also among the worst localized in the sample and suffer from limited galaxy-catalog coverage, which plausibly contributes to their broader H_0 posteriors. The peaks seen in the individual H_0 posteriors reflect overdensities in the redshift distribution of potential host galaxies along each GW line of sight, and the width of each peak depends on the precision of the galaxy photo- z PDFs and on the size of the GW localization volume, which sets the number of potential host galaxies over which the marginalization is performed.

We quantify the impact of adding fake galaxies for the three GW events that require them (GW230731_215307, GW230919_215712, and GW230927_153832). For individual events, the inclusion of fake galaxies flattens the H_0 posteriors, increasing the uncertainty by approximately 4%–9%. When these events are combined with the full dark siren sample, the effect on the H_0 constraint becomes much smaller: the posterior mode shifts by at most $\sim 2\%$, and the uncertainties increase by no more than $\sim 1\%$ across all configurations explored in our analysis. No significant change is found when the results are combined with the bright siren GW170817.

We find statistical agreement with our previous results using the same configuration (no luminosity weighting and a Gaussian GW likelihood), when the five dark sirens had not yet been confirmed as GW events.

In this analysis, the photo- z model for the two GW events in the northern hemisphere (GW230627_015337 and GW231226_101520) was trained using only galaxies from the northern footprint of the LS DR9, whereas the previous work used a combined north and south DR9 training sample. This change alters the redshift distribution of potential host galaxies, shifting the mean redshift by $\Delta z_{\text{mean}} = -0.037$ for GW230627 and $\Delta z_{\text{mean}} = 0.046$ for GW231226. Nevertheless, the resulting H_0 posterior remains consistent with our previous results within statistical uncertainties. The updated sky maps yield modestly improved 90% CI areas, while in most cases the luminosity distance uncertainties are slightly larger. We found that these updates lead to tighter H_0 uncertainties, with relative reductions ranging from approximately 1% to 23% for the individual events, indicating that improvements in sky localization tend to have a larger impact than variations in the luminosity distance uncertainty.

A. Luminosity weighting effect

We now investigate the impact of r -band luminosity weighting on the individual H_0 posteriors and their combined constraint. Uncertainties in the apparent magnitudes of host galaxies have a negligible impact on the inferred H_0 posterior. The relative difference is below the 0.01% level, and the apparent magnitude integral computed assuming perfect measurements differs from the result including magnitude uncertainties by at most $\mathcal{O}(10^{-6})$. The two results are therefore numerically indistinguishable, indicating that neglecting apparent magnitude errors does not affect the subsequent H_0 inference.

For the events GW230731_215307, GW230919_215307, and GW230927_153832, synthetic galaxies are injected as described in Section III B. Since our deep learning model estimates only photo- z , their apparent magnitudes are assigned through an empirical $m(z)$ relation derived from the training sample rather than a joint luminosity-redshift distribution. We find that applying luminosity weighting systematically shifts the host redshift distribution toward higher z . To avoid introducing this potential bias in the H_0 inference, we adopt a conservative approach and assign equal weights to the synthetic galaxies when computing the final H_0 posterior.

Overall, luminosity weighting modifies the redshift distribution of potential host galaxies by shifting the peak toward slightly higher redshift, with typical displacements of $\Delta z \sim 0.01$ – 0.1 , and by making the distribution more concentrated (i.e., with a reduced effective width), as illustrated by the comparison between the blue and orange curves in Fig. 8. These changes propagate into the inferred H_0 posterior. The overall structure of the posterior is largely preserved, with luminosity weighting primarily reweighting existing modes rather than significantly modifying its shape (see the comparison between the orange and blue curves in Fig. 4). Quantitatively, the Kullback–Leibler (KL) divergence [128] be-

tween the weighted and unweighted posteriors ranges between $D_{\text{KL}} \simeq 0.005$ and 0.39 across the analyzed events, indicating moderate redistributions of probability density without qualitatively altering the posterior structure.

In several events, luminosity weighting shifts the H_0 posterior toward lower values, despite shifting the redshift distribution toward higher z . This behavior is observed, for example, in GW230627_015337, GW230922_020344, and GW231206_233901. Nevertheless, the overall impact of luminosity weighting remains subdominant relative to other elements of the methodology (see the discussion in App. A).

In the luminosity-weighted analysis, combining the seven dark sirens from the O4a observing run with the ten events from previous runs and studies [45, 47, 50, 91] yields $H_0 = 78.2^{+12.0}_{-11.0}$ km/s/Mpc when using the full GW likelihood (see blue solid line in Fig. 6), and $H_0 = 72.8^{+12.6}_{-14.3}$ km/s/Mpc when the GW likelihood is approximated by a Gaussian. These measurements are consistent within 1σ with each other and independent determinations of H_0 , including those from SH0ES, Planck, and the GWTC-4 dark siren analysis. In Fig. 5 we compare the luminosity-weighted and unweighted H_0 posteriors. When using the full GW likelihood, the inclusion of luminosity weighting reduces the uncertainty on H_0 by 1.9 km/s/Mpc, corresponding to an improvement of $\sim 14\%$.

Figure 6 presents our main results (summarized in Table II), shown as blue solid and dashed lines for the 17 dark sirens analyzed with the full GW likelihood. The combination of the bright siren GW170817 measurement (gray line), which accounts for peculiar velocity corrections and includes the inclination constraint from VLBI data [127], with the luminosity-weighted dark siren posterior yields $H_0 = 69.9^{+4.1}_{-4.0}$ km/s/Mpc, and is shown as the black solid line in Fig. 6. The dark siren information provides a slightly broader posterior, with an improvement of 11% in the uncertainty compared to the bright siren alone. Our results are broadly consistent within 1σ with those reported by the Planck [25] and SH0ES collaboration [26] measurements.

In addition, we compare our results with previous dark siren analyses based on the latest GW catalog release [53, 68, 72]. Here, we focus the comparison on our full GW likelihood result, since it is more directly comparable to previous analyses that also marginalize over the BBH mass population. Our result, based on the full GW likelihood, is broadly consistent with those studies, but we obtain a competitive and precise constraint despite the smaller number of events considered (see Table II). The larger difference between our uncertainties and those reported in Abac and et al. [52] arises primarily because they infer H_0 jointly with the BBH mass-population parameters, whereas in our analysis these parameters are fixed. Fixing the population parameters leads to more optimistic constraints, as also seen in the GWTC-3 results. The impact of this coupling additionally depends on the choice of BBH mass model. Pierra and Papadopoulos [53], who adopt the same inference

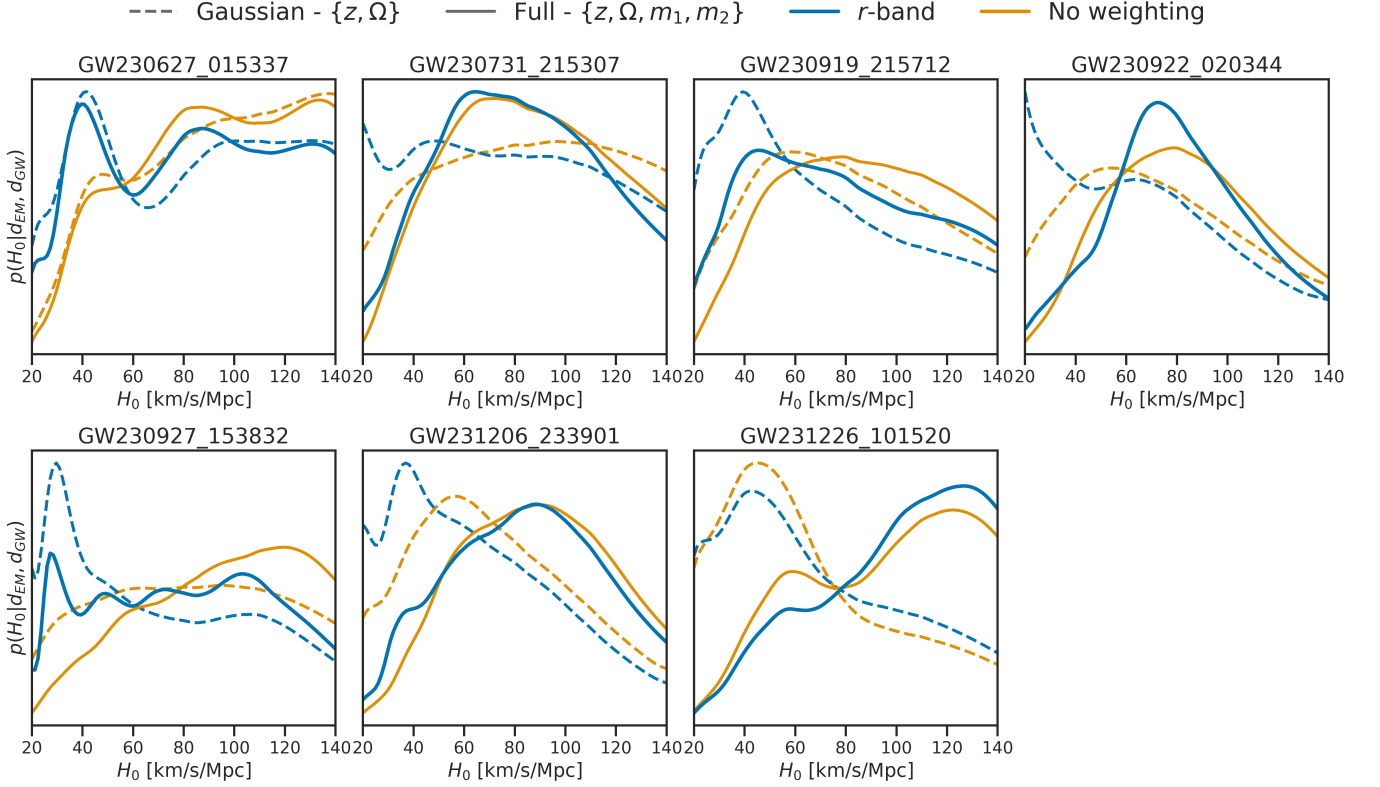


FIG. 4. Posterior distributions of the Hubble constant inferred from individual gravitational wave events. Solid lines represent the analysis using the full GW likelihood, and dashed lines represent the Gaussian approximation. Blue curves correspond to r -band weighted results, while orange curves are unweighted.

TABLE II. Hubble constant constraints obtained from GW standard sirens, presented in this work and in the literature. All H_0 measurements and uncertainties are reported in km/s/Mpc. Reported uncertainties represent the 68% highest-density interval around the posterior maximum. The value shown in parentheses indicates the relative precision, defined as σ_{H_0}/H_0 . For dark siren analyses employing population modeling, “PLP” denotes the *Power-Law + Peak* mass model [122, 123], and the semiparametric B-spline mass model corresponds to that introduced by Edelman et al. [124, 125]. The “BPL+3peak” model is based on the “FullPop-4.0” compact binary population model [52, 107], in which the broken power-law mass spectrum is supplemented with three Gaussian components (Pierra and Papadopoulos 53, hereafter BPL+3peak). References: (1) Abbott et al. [120], (2) Abac and et al. [52], (3) Pierra and Papadopoulos [53], (4) Tagliacuzzi et al. [68], (5) Bom et al. [51], (6) adapted from Nicolaou et al. [126], (7) Mukherjee et al. [127], and (8) this work.

Event(s)	Method(s)	H_0 (km/s/Mpc)	σ_{H_0} (km/s/Mpc)
O1-O3 – 47 dark sirens ¹	Catalog (K-band luminosity-weighted) + BNS/NSBH/BBH population (PLP model with fixed parameters)	67^{+13}_{-12}	12.5 (18%)
O1-O4a – 142 dark sirens ²	Catalog (K-band luminosity-weighted) + BNS/NSBH/BBH population (FullPop-4.0 model)	$81.6^{+21.5}_{-15.9}$	18.7 (23%)
O1-O4a – 142 dark sirens ³	Catalog (K-band luminosity-weighted) + BNS/NSBH/BBH population (BPL+3peak model)	$82.5^{+16.8}_{-14.3}$	15.6 (19%)
O1-O4a – 142 dark sirens ²	BNS/NSBH/BBH population (FullPop-4.0 model)	$76.4^{+25.0}_{-18.1}$	20.6 (27%)
O1-O4a – 137 dark sirens ⁴	BBH population (semiparametric B-spline model)	$57.8^{+21.9}_{-20.6}$	21.3 (37%)
O1-O4a – 15 dark sirens ⁵	Catalog (no luminosity weighting)	$70.4^{+13.6}_{-11.7}$	12.6 (18%)
GW170817 ⁶	Bright (v_p corrected)	$68.8^{+17.3}_{-7.6}$	12.5 (18%)
GW170817 ⁷	Bright (v_p +VLBI)	$68.3^{+4.6}_{-4.5}$	4.6 (7%)
O1-O4a – 17 dark sirens ⁸	Catalog (no luminosity weighting; GW likelihood Gaussian approximation, eq. 5)	$72.6^{+11.6}_{-13.2}$	11.4 (16%)
O1-O4a – 17 dark sirens ⁸	Catalog (r -band luminosity-weighted; GW likelihood Gaussian approximation, eq. 5)	$72.8^{+13.2}_{-14.3}$	13.5 (18%)
O1-O4a – 17 dark sirens ⁸	Catalog (no luminosity weighting; full GW likelihood, eq. 6)	$78.8^{+12.2}_{-12.0}$	13.4 (17%)
O1-O4a – 17 dark sirens ⁸	Catalog (r -band luminosity-weighted; full GW likelihood, eq. 6)	$78.2^{+12.0}_{-11.0}$	11.5 (15%)
O1-O4a – 17 dark + 1 bright siren ⁸	Bright (host) + Catalog (r -band luminosity-weighted; full GW likelihood, eq. 6)	$75.2^{+8.0}_{-7.0}$	8.0 (11%)
O1-O4a – 17 dark + 1 bright siren (EM) ⁸	Bright (v_p +VLBI) + Catalog (r -band luminosity-weighted; full GW likelihood, eq. 6)	$69.9^{+4.1}_{-4.0}$	4.1 (6%)

framework as Abac and et al. [52] but use a better-fitting mass model (BPL+3peak, with a Bayes factor of 6 over the FullPop-4.0 model used in [52] when reweighted by the effective prior volume), report an improvement in the H_0 uncertainty of 36.2% relative to Abac and et al. [52], yielding an uncertainty comparable to that obtained in

our analysis.

In previous studies [52, 53, 120], the contribution from galaxy information has been found to be small compared to that from the BBH mass distribution, leading to improvements of only ~ 7 –9% in the H_0 uncertainty. This lack of information can be understood by the choice

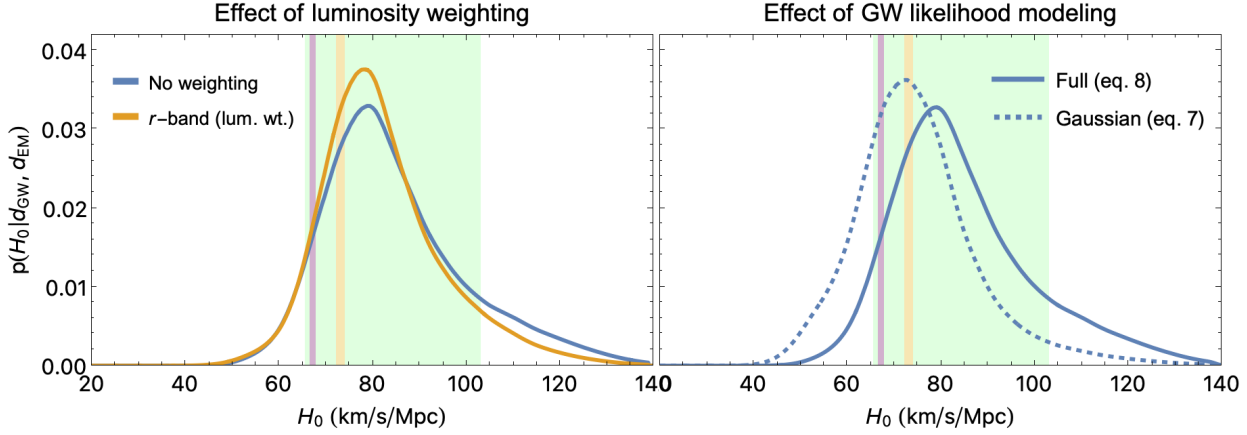


FIG. 5. **Left panel:** effect of galaxy-catalog weighting, with the full GW likelihood held fixed. The blue curve shows the result with no weighting, the orange curve uses r -band luminosity weighting, and the green curve uses g -band luminosity weighting. **Right panel:** effect of the GW likelihood treatment using the unweighted catalog. The solid blue curve corresponds to the full GW likelihood (as defined in eq. 6), while the dashed blue curve shows the Gaussian approximation likelihood (see eq. 5). In both panels, shaded regions indicate the 68% CI on H_0 from the Planck CMB inference [25] (pink), the SH0ES distance-ladder measurement [26] (yellow), and the GWTC-4 dark siren analysis based on 142 events with the FullPop-4.0 population model [52] (green).

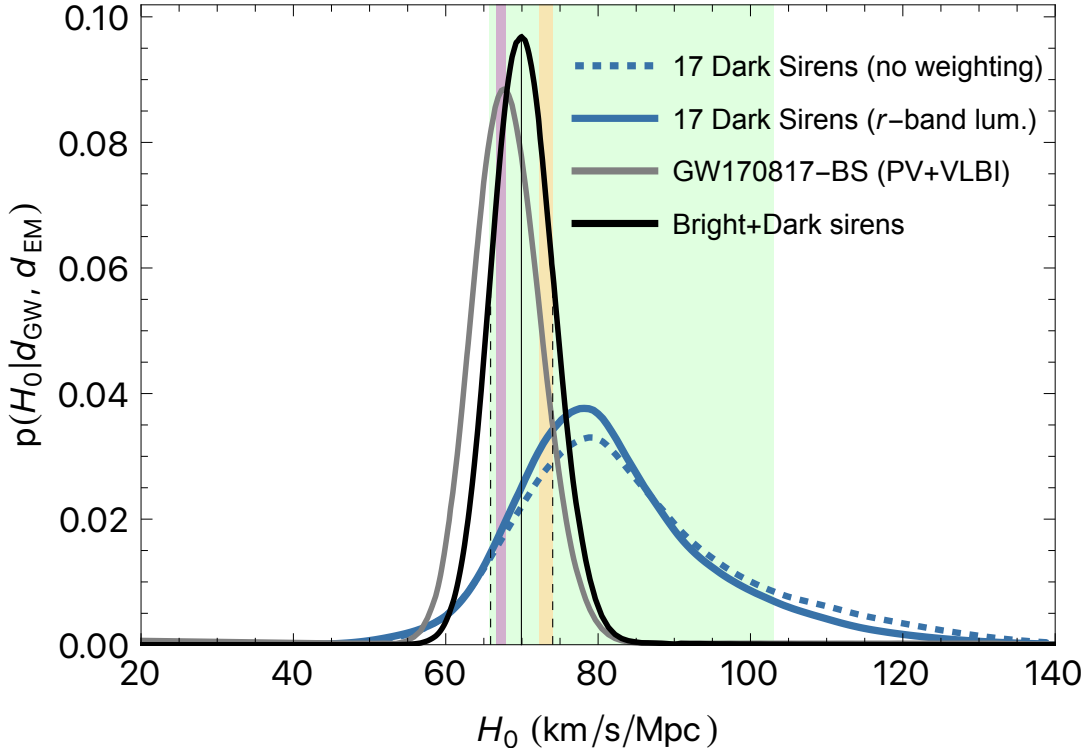


FIG. 6. Hubble constant posterior inferred from dark and bright GW standard sirens. The blue curves show the constraints from the 17 dark sirens observed during O1–O4a and analyzed in this work using the full GW likelihood: the solid blue line corresponds to the result obtained with r -band luminosity weighting of the galaxy catalog, while the dashed blue line assumes equal weights. The gray curve shows the bright siren measurement from GW170817 using the GW+VLBI data with peculiar velocity corrections [127]. The black curve represents the joint constraint from combining the bright siren with the luminosity-weighted dark siren sample. For reference, shaded regions indicate the 1σ intervals from the Planck CMB inference [25] (pink), the SH0ES distance-ladder measurement [26] (yellow), and the GWTC-4 dark siren analysis based on 142 events with the FullPop-4.0 population model [52] (green).

of galaxy catalogs employed: those analyses relied on the GLADE+ catalog [129], which becomes highly incomplete and inhomogeneous at the distances typical of GWTC-4 events, well beyond its completeness limit of $\sim 47_{-2}^{+4}$ Mpc, leaving most events with insufficient support in the redshift range of interest. Therefore, following previous works [47, 50, 51], we restrict our analysis to well-localized events that lie within the completeness range of the DESI imaging survey, thereby avoiding the lack of redshift support that would otherwise yield a weakly constrained H_0 posterior.

B. Effect of the BBH mass posteriors on the GW likelihood

In this subsection, we investigate how different implementations of the GW likelihood impact the dark siren inference of H_0 . For almost all GW events considered, we find that the full likelihood consistently shifts the peak of the H_0 posterior toward higher values compared to the Gaussian approximation, highlighting the impact of the two different GW likelihood implementations (see Fig. 4, where the unweighted case is shown in orange, and the dashed and solid curves correspond to the Gaussian and full likelihoods, respectively). Combining the 17 dark siren events and assuming equal probability for all possible host galaxies, we obtain $H_0 = 72.6_{-11.3}^{+11.6}$ km/s/Mpc using the Gaussian likelihood, while the full likelihood yields $H_0 = 78.8_{-12.2}^{+14.6}$ km/s/Mpc. These results are statistically consistent with each other within their respective uncertainties and are shown in the right panel of Fig. 5, indicating that the Gaussian approximation to the GW likelihood can still yield a consistent H_0 inference.

The behavior seen in Fig. 7 is influenced by the inclusion of the BBH population mass prior in the GW likelihood. The mass model adopted in this work follows a broken power-law with two peaks for the primary black hole mass, with characteristic scales at $\sim 10 M_\odot$ and $\sim 35 M_\odot$, and therefore favors source-frame primary masses near these values. For any GW event, only specific combinations of z and H_0 map the inferred source-frame masses, $m_i = m_{i,\text{det}}/(1+z)$, into the preferred regions of the population mass distribution.

Figure 7 illustrates this effect for GW230922_020344 by comparing the GW likelihood obtained using the BBH broken power-law + two-peaks mass model to that obtained assuming a flat mass prior. The inclusion of the mass prior redistributes probability in the (z, H_0) plane, enhancing regions where the inferred source-frame masses align with the preferred population scales and suppressing others. This demonstrates how the assumed mass model directly shapes the (z, H_0) dependence of the GW likelihood and, consequently, the inferred H_0 posterior. As a result, likelihood support is reduced at low H_0 and low z (blue regions) and enhanced at higher H_0 and redshift (red regions), shifting the inferred H_0 posterior

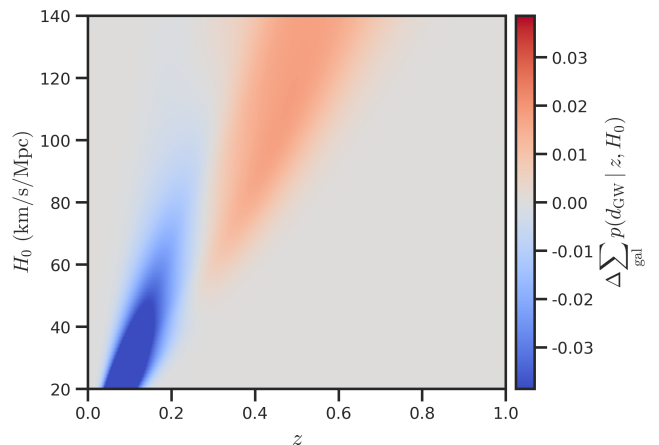


FIG. 7. Difference in the galaxy-summed GW likelihood, $\Delta \sum_{N_{\text{gal}}} p(d_{\text{GW}} | z, H_0)$, between analyses using the BBH broken power-law + two-peaks mass model and assuming a flat source-frame mass prior for the event GW230922_020344. Both likelihood surfaces are normalized over the full (z, H_0) plane before differencing, so the map highlights only changes in the shape of the GW likelihood induced by the mass model. Red (blue) regions indicate where the mass model increases (decreases) the GW likelihood.

toward higher values.

C. Electromagnetic selection effects in dark siren analysis

To quantify the impact of electromagnetic selection on the dark siren H_0 inference, we compare two selection functions, as described in Section III A: (1) one that includes only the GW detection cuts, assuming all galaxies are observable within the survey sensitivity at the distances of the dark siren events considered in this work, and (2) one that incorporates both the GW cuts and the incompleteness of the magnitude-limited galaxy catalog. The comparison of individual H_0 posteriors computed using the two selection functions reveals only a percent-level shift in the posterior mode, with uncertainties remaining $\lesssim 3\%$ for all dark siren events and configurations explored. We further quantify the difference between the posteriors using the KL divergence, finding $D_{\text{KL}} < 3 \times 10^{-3}$, which indicates that the two distributions are nearly indistinguishable in both shape and information content. These small differences indicate that assuming all galaxies are observable within the survey sensitivity is a good approximation, yielding H_0 constraints that are fully consistent with each other and well within the statistical uncertainty.

V. CONCLUSIONS

In this work, we present a revised measurement of the Hubble constant using the statistical dark siren method, combining the best localized events from the O4a observing run of the LVK network in the GWTC-4 catalog with galaxy photometric data from the LS. Our analysis focuses on several key methodological aspects: in the electromagnetic component, the treatment of galaxy photometric redshifts and luminosity weighting, and in the GW component, alternative implementations of the GW likelihood. We investigate how these choices affect the inferred H_0 posteriors for both individual events and their combination.

Using a sample of 17 dark siren events, seven from the O4a observing run and the other ten from previous runs analyzed in Soares-Santos et al. [45], Alfradique et al. [50], Bom et al. [51], Palmese et al. [91], we obtain a constraint of $H_0 = 78.8^{+14.6}_{-12.2}$ km/s/Mpc corresponding to a precision of approximately 17%, when using the full GW posterior information and assuming no luminosity weighting for the potential host galaxies. When the GW likelihood is instead approximated by a Gaussian distribution, thereby neglecting information from the binary black hole component masses, we obtain a consistent constraint of $H_0 = 72.6^{+11.6}_{-11.3}$ km/s/Mpc. The two measurements are in good agreement, with the full GW likelihood yielding a slightly higher posterior maximum, primarily due to the fixed BBH mass population prior adopted in the analysis.

The inclusion of r -band luminosity weighting leads to percent-level changes in the H_0 constraints for most individual events. In the combined analysis of the 17 dark sirens, luminosity weighting broadens the 68% CI by $\sim 18\%$ when the GW likelihood is approximated by a Gaussian, but reduces it by $\sim 14\%$ when the full GW likelihood is used. We also assess the impact of including uncertainties in the apparent magnitudes of galaxies and find no statistically significant effect on the results. This indicates that, at the current level of precision, these magnitudes can be safely treated as perfectly measured. The resulting luminosity-weighted constraint is $H_0 = 78.2^{+12.0}_{-11.0}$ km/s/Mpc, consistent within uncertainties with the result obtained without luminosity weighting. This is in agreement with previous studies showing that biases from fixing a host-galaxy weighting scheme can be safely neglected for complete galaxy catalogs and well-localized events [118, 130, 131]. Nevertheless, this does not exclude the possibility that such choices may introduce systematic biases in other observational configurations [130, 132].

Finally, we combine our 17 dark siren measurements obtained with r -band luminosity weighting with the bright siren GW170817, taking into account constraints from VLBI measurements of the viewing angle and corrections for the host galaxy peculiar velocity [127], to obtain a combined constraint of $H_0 = 69.9^{+4.1}_{-4.0}$ km/s/Mpc. This result represents an improvement of approximately

67% and 64% in uncertainty compared to the measurements obtained using the GW170817 bright siren result with only peculiar velocity corrections [126] and using dark sirens alone, respectively. Although the bright siren provides the dominant constraint, adding the dark sirens to the GW170817 measurement still reduces the uncertainty by about 11%, illustrating the complementarity between bright and dark sirens in GW cosmology.

The H_0 constraints presented here rely on fixed assumptions about the BBH merger rate and population mass distribution, adopted to enable a direct comparison with the methodology used in previous works [45, 50, 51, 78, 91]. In particular, we model the BBH merger rate as tracing the r -band luminosity of galaxies, motivated by its correlation with stellar mass, and we neglect the time delay between the formation of stellar progenitors and the BBH merger. Binary population synthesis simulations combined with galaxy evolution models [95, 96, 98, 133, 134] have shown, however, that the merger rate depends not only on stellar mass, but also on star formation rate and metallicity. We leave this investigation to future work. In upcoming GW observing runs, the expected increase in the number of well-localized dark siren events, together with the advent of deeper wide-field galaxy surveys such as the Vera C. Rubin Observatory Legacy Survey of Space and Time [135], and possible additional bright siren detections, is expected to bring GW cosmology to percent-level precision, where controlling systematic effects will become essential.

ACKNOWLEDGEMENTS

The authors made use of Sci-Mind servers machines developed by the CBPF AI LAB team and would like to thank Paulo Russano and Marcelo Portes de Albuquerque for all the support in infrastructure matters. CRB acknowledges the financial support from CNPq (316072/2021-4) and from FAPERJ (grants 201.456/2022 and 210.330/2022) and the FINEP contract 01.22.0505.00 (ref. 1891/22). AS acknowledges the financial support from CNPq (402577/2022-1). GT acknowledges the financial support from CNPq (PhD fellowship, 140212/2022-1) and from FAPERJ (PhD merit fellowship - FAPERJ NOTA 10, 202.432/2024).

The Legacy Surveys consist of three individual and complementary projects: the Dark Energy Camera Legacy Survey (DECaLS; NSF's OIR Lab Proposal ID 2014B-0404; PIs: David Schlegel and Arjun Dey), the Beijing-Arizona Sky Survey (BASS; NSF's OIR Lab Proposal ID 2015A-0801; PIs: Zhou Xu and Xiaohui Fan), and the Mayall z -band Legacy Survey (MzLS; NSF's OIR Lab Proposal ID 2016A-0453; PI: Arjun Dey). DECaLS, BASS and MzLS together include data obtained, respectively, at the Blanco telescope, Cerro Tololo Inter-American Observatory, The NSF's National Optical-Infrared Astronomy Research Laboratory (NSF's OIR Lab); the Bok telescope, Steward Observatory, Univer-

sity of Arizona; and the Mayall telescope, Kitt Peak National Observatory, NSF’s OIR Lab. The Legacy Surveys project is honored to be permitted to conduct astronomical research on Iolkam Du’ag (Kitt Peak), a mountain with particular significance to the Tohono O’odham Nation.

The NSF’s OIR Lab is operated by the Association of Universities for Research in Astronomy (AURA) under a cooperative agreement with the National Science Foundation.

This project used data obtained with the Dark Energy Camera (DECam), which was constructed by the Dark Energy Survey (DES) collaboration. Funding for the DES Projects has been provided by the U.S. Department of Energy, the U.S. National Science Foundation, the Ministry of Science and Education of Spain, the Science and Technology Facilities Council of the United Kingdom, the Higher Education Funding Council for England, the National Center for Supercomputing Applications at the University of Illinois at Urbana-Champaign, the Kavli Institute of Cosmological Physics at the University of Chicago, Center for Cosmology and Astro-Particle Physics at the Ohio State University, the Mitchell Institute for Fundamental Physics and Astronomy at Texas A&M University, Financiadora de Estudos e Projetos, Fundacao Carlos Chagas Filho de Amparo, Financiadora de Estudos e Projetos, Fundacao Carlos Chagas Filho de Amparo a Pesquisa do Estado do Rio de Janeiro, Conselho Nacional de Desenvolvimento Cientifico e Tecnolico and the Ministerio da Ciencia, Tecnologia e Inovacao, the Deutsche Forschungsgemeinschaft and the Collaborating Institutions in the Dark Energy Survey. The Collaborating Institutions are Argonne National Laboratory, the University of California at Santa Cruz, the University of Cambridge, Centro de Investigaciones Energeticas, Medioambientales y Tecnologicas-Madrid, the University of Chicago, University College London, the DES-Brazil Consortium, the University of Edinburgh, the Eidgenossische Technische Hochschule (ETH) Zurich, Fermi National Accelerator Laboratory, the University of Illinois at Urbana-Champaign, the Institut de Ciencies de l’Espai (IEEC/CSIC), the Institut de Fisica d’Altes Energies, Lawrence Berkeley National Laboratory, the Ludwig-Maximilians Universitat Munchen and the associated Excellence Cluster Universe, the University of Michigan, the National Optical Astronomy Observatory, the University of Nottingham, the Ohio State University, the University of Pennsylvania, the University of Portsmouth, SLAC National Accelerator Laboratory, Stanford University, the University of Sussex, and Texas A&M University.

BASS is a key project of the Telescope Access Program (TAP), which has been funded by the National Astronomical Observatories of China, the Chinese Academy of Sciences (the Strategic Priority Research Program “The Emergence of Cosmological Structures” Grant # XDB09000000), and the Special Fund for Astronomy from the Ministry of Finance. The BASS is also sup-

ported by the External Cooperation Program of Chinese Academy of Sciences (Grant # 114A11KYSB20160057), and Chinese National Natural Science Foundation (Grant # 11433005).

The Legacy Survey team makes use of data products from the Near-Earth Object Wide-field Infrared Survey Explorer (NEOWISE), which is a project of the Jet Propulsion Laboratory/California Institute of Technology. NEOWISE is funded by the National Aeronautics and Space Administration.

The Legacy Surveys imaging of the DESI footprint is supported by the Director, Office of Science, Office of High Energy Physics of the U.S. Department of Energy under Contract No. DE-AC02-05CH1123, by the National Energy Research Scientific Computing Center, a DOE Office of Science User Facility under the same contract; and by the U.S. National Science Foundation, Division of Astronomical Sciences under Contract No. AST-0950945 to NOAO.

The Photometric Redshifts for the Legacy Surveys (PRLS) catalog used in this paper was produced thanks to funding from the U.S. Department of Energy Office of Science, Office of High Energy Physics via grant DE-SC0007914.

DATA AVAILABILITY

The data underlying this article will be shared on reasonable request to the corresponding author.

Appendix A: Effects of photo- z non-Gaussianity and luminosity weighting on individual H_0 posteriors

In this appendix, we examine the impact of approximating galaxy redshift measurements with a Gaussian distribution on the inferred H_0 posteriors. We also analyze how applying r -band luminosity weighting modifies the redshift distributions of potential host galaxies and propagates into the H_0 inference for individual dark siren events.

In most dark siren analyses, galaxy photometric redshift uncertainties are modeled using a Gaussian approximation [see, e.g., 45, 52, 78, 120]. As shown by Turски et al. [136], neglecting redshift uncertainties can introduce a bias comparable to other known systematic effects, although still much smaller than the dominant statistical uncertainty in GWTC-3 constraints. Consequently, the choice of redshift error model does not significantly affect the current precision of the Hubble constant measurement. However, the use of the full photo- z probability density functions (here estimated with the MDN technique; see section II C) offers an important advantage: by naturally capturing the multiple peak structures arising from color-redshift degeneracies, it yields a more accurate description of small scale features in the redshift distribution $N(z)$, as shown by Palmese et al. [91],

and as already established in several studies of photometric survey analyses [137–139]. Another important aspect is that the Gaussian photo- z approximation also introduces a dependence on the redshift cuts applied to the volume-limited sample, due to the non-negligible contribution of its tails at high redshift (and hence high H_0), as discussed by Soares-Santos et al. [45] and evidenced in Palmese et al. [91]. Although systematic effects associated with the Gaussian photo- z approximation have not yet been widely explored, their impact may become more important as the precision of dark siren measurements improves. As galaxy catalogs become more complete and the number of GW detections increases, reducing the statistical errors, such systematics could become statistically relevant for H_0 inference.

We focus on comparing the H_0 posterior distributions obtained using the full photo- z probability density functions estimated with the MDN approach adopted in this work with those based on a Gaussian approximation. In the latter case, each galaxy photo- z PDF is replaced by a Gaussian distribution whose mean and standard deviation are set to match the peak and the width of the corresponding full photo- z PDF, respectively. We explore this comparison across all configurations adopted in this work: (i) equal versus r -band luminosity weighting, and (ii) the full versus Gaussian implementations of the GW likelihood. Figure 8 shows the redshift distributions of potential host galaxies obtained using either the full MDN photo- z PDFs (solid lines) or their Gaussian approximations (dashed lines). For most configurations in the no-weighting case, the Gaussian approximation produces no statistically significant change in the shape of the resulting H_0 posteriors, with the solid and dashed orange curves nearly overlapping. An exception occurs for GW230627_015337 and GW231226_101520, where the Gaussian approximation yields a slightly more precise H_0 constraint and introduces a small shift in its peak, both below the 1% level.

The greatest impact occurs when r -band luminosity weighting is applied, with the strongest effects observed for GW230627_015337, GW230922_020344, and GW231226_101220, as evident in Fig. 8. The Gaussian approximation leads to noticeable shifts in the credible intervals, which propagate directly to the inferred H_0 posterior. For GW230922_020344, it shifts the posterior peak from 20.0 km/s/Mpc to 68.5 km/s/Mpc, with a $\sim 5\%$ reduction in the 68% CI when the GW likelihood is approximated as Gaussian. An even larger effect is observed for GW230627_015337, where the posterior mode shifts by $\sim 91(47)$ km/s/Mpc for the Gaussian (full) GW likelihood case, while the uncertainty decreases by 5%(6%). In GW231226_101220, the approximation instead modifies the H_0 uncertainty, increasing (decreasing) it by about 5% in the Gaussian (full) GW likelihood

case. These deviations highlight the importance of accounting for non-Gaussian features in the photo- z PDFs and indicate that Gaussian approximations can introduce systematic biases in individual dark siren H_0 inferences. This motivates further investigation with realistic simulations and different observing scenarios for galaxy surveys and GW detections, which we plan to explore in future work.

We now examine the effect of r -band luminosity weighting on the host galaxy redshift distributions and the resulting H_0 inference. For GW230627_015337, we find that luminosity weighting broadens the redshift distribution of potential host galaxies, which in turn flattens the joint GW–EM likelihood and increases the relative contribution of the redshift prior in the marginalization over z . When marginalized over redshift, this term peaks at low H_0 because the comoving volume element scales as $dV/dz \propto H_0^{-3}$ at fixed z . At low H_0 , the likelihood still retains non-negligible support, but the redshift prior increases the relative weight of these regions in the marginalization, driving the inference toward smaller H_0 values. The effect becomes more pronounced when luminosity weighting is applied, as it broadens the joint GW–EM likelihood for GW230627_015337, reducing the information gain relative to the prior from $D_{\text{KL}} = 1.02$ to 0.75. This behavior is illustrated in the top panel of Fig. 9. The left panel shows the joint GW–EM likelihood in the (z, H_0) plane, which is not maximal at low H_0 (e.g., $H_0 \simeq 40$ km/s/Mpc) but still retains non-negligible support. The right panel shows the same likelihood weighted by the redshift prior $p(z, H_0) \propto dV/dz$, clearly enhancing the probability toward smaller values of H_0 .

For GW230922_015337, using the Gaussian approximation to the GW likelihood (dashed lines in Fig. 4), we find that the H_0 posterior in the no-weighting case peaks at $H_0 \simeq 50$ km/s/Mpc. In contrast, the luminosity-weighted case shows a broader distribution with a secondary peak near $H_0 \simeq 68$ km/s/Mpc, but with higher probability density toward lower values around $H_0 \simeq 20$ km/s/Mpc. This shift is driven by the change in the redshift distribution of potential host galaxies: the no-weighting case (orange curve in Fig. 8) peaks at $z \simeq 0.3$, whereas the luminosity-weighting case (blue curve) peaks at $z \simeq 0.4$. The extended tail toward low H_0 arises from the high- z tail of the photometric redshift PDFs modeled with the MDN methodology. The non-Gaussian features in the photo- z PDFs significantly affect the shape of the redshift distribution along the line of sight in the luminosity-weighting scenario. This is illustrated in the bottom panel of Fig. 9, where the MDN-based case (right) shows non-zero probability at $H_0 \simeq 20$ km/s/Mpc for high z , in contrast to the Gaussian photo- z approximation (left).

[1] A. Perego, S. Rosswog, R. M. Cabezón, and et al., Neutrino-driven winds from neutron star merger rem-

nants, *MNRAS* **443**, 3134–3156 (2014).

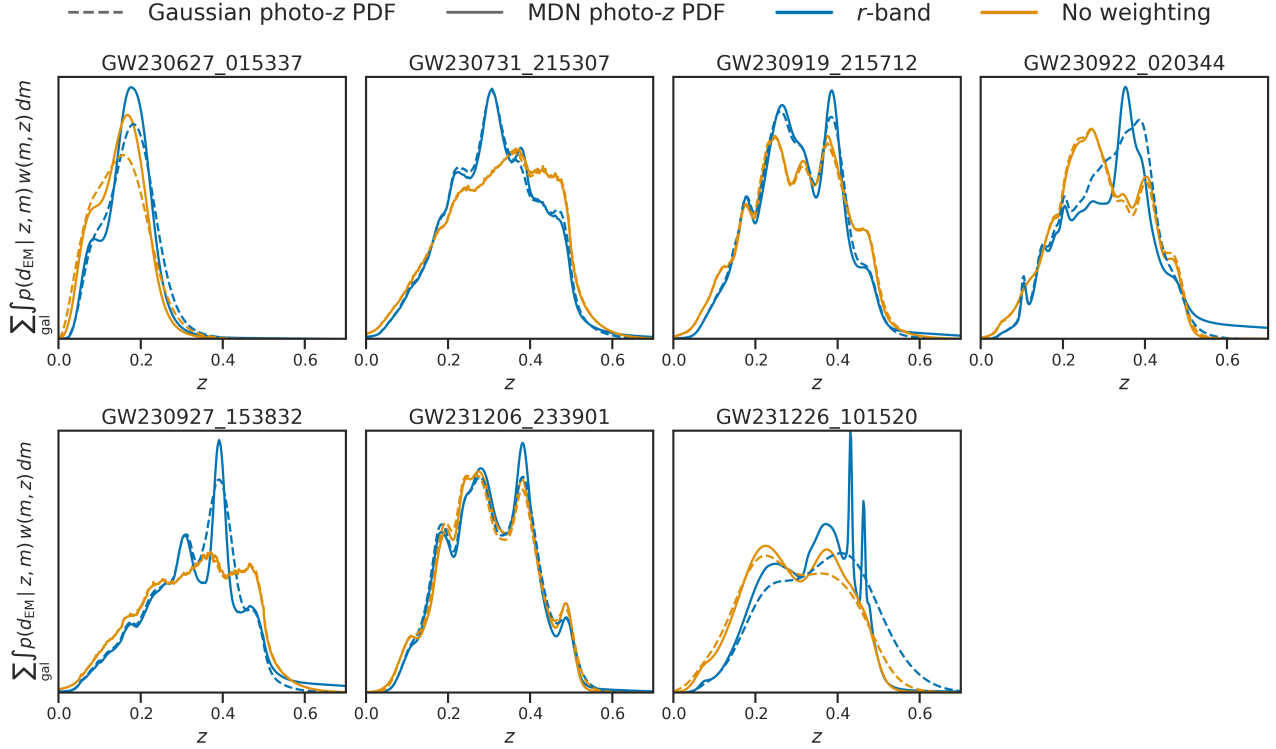


FIG. 8. Redshift distributions of possible host galaxies for individual GW events. Each panel shows the sum over galaxies of the integrated product of the electromagnetic likelihood and the galaxy host weighting as a function of redshift z . Solid lines correspond to the photo- z PDFs obtained with the MDN method, while dashed lines correspond to the Gaussian approximation. The colors indicate the weighting scheme: r -band luminosity weighting (blue) and unweighted (orange). The distributions are normalized to unity in each panel for better visual comparison.

- [2] S. S. Kimura, K. Murase, P. Mészáros, and K. Kiuchi, High-energy neutrino emission from short gamma-ray bursts: Prospects for coincident detection with gravitational waves, *ApJL* **848**, L4 (2017).
- [3] K. Fang and B. D. Metzger, High-energy neutrinos from millisecond magnetars formed from the merger of binary neutron stars, *ApJ* **849**, 153 (2017).
- [4] D. Biehl, J. Heinze, and W. Winter, Expected neutrino fluence from short gamma-ray burst 170817a and off-axis angle constraints, *MNRAS* **476**, 1191–1197 (2018).
- [5] R. Abbasi, M. Ackermann, J. N. Adams, J. A. Aggarwal, and et al. (IceCube Collaboration), Icecube search for neutrinos coincident with gravitational wave events from ligo/virgo run o3, *ApJ* **944**, 80 (2023).
- [6] M. Mukhopadhyay, S. S. Kimura, and K. Murase, Gravitational wave triggered searches for high-energy neutrinos from binary neutron star mergers: Prospects for next generation detectors, *Phys. Rev. D* **109**, 043053 (2024).
- [7] A. Janiuk, Nucleosynthesis of elements in gamma-ray burst engines, *A&A* **568**, 7 (2014).
- [8] D. Kasen, B. Metzger, J. Barnes, and et al., Origin of the heavy elements in binary neutron-star mergers from a gravitational-wave event, *Nature* **551**, 80–84 (2017).
- [9] M. W. Coughlin, T. Dietrich, B. Margalit, and B. D. Metzger, Multimessenger bayesian parameter inference of a binary neutron star merger, *MNRAS Lett.* **489**, L91–L96 (2019).
- [10] T. Dietrich, M. W. Coughlin, P. T. H. Pang, and et al., Multimessenger constraints on the neutron-star equation of state and the hubble constant, *Science* **370**, 1450 (2020).
- [11] M.-H. Chen, L.-X. Li, Q.-H. Chen, and et al., Neutron star mergers as the dominant contributor to the production of heavy r -process elements, *MNRAS* **529**, 1154 (2024).
- [12] A. G. Abac, I. Abouelfettouh, F. Acernese, and et al. (The LIGO Scientific Collaboration, The Virgo Collaboration, and The KAGRA Collaboration), Black hole spectroscopy and tests of general relativity with gw250114, *Phys. Rev. Lett.* **136**, 041403 (2026).
- [13] R. Abbott, H. Abe, F. Acernese, and et al. (LIGO Scientific Collaboration, Virgo Collaboration, and KAGRA Collaboration), Tests of general relativity with gwtc-3, *Phys. Rev. D* **112**, 084080 (2025).
- [14] D. Radice, A. Perego, F. Zappa, and S. Bernuzzi, Gw170817: Joint constraint on the neutron star equation of state from multimessenger observations, *ApJL* **852**, L29 (2018).
- [15] B. P. Abbott, R. Abbott, T. D. Abbott, and et al., Gw170817: Measurements of neutron star radii and equation of state, *Phys. Rev. Lett.* **121**, 161101 (2018).
- [16] C. A. Raithel, Constraints on the neutron star equation of state from gw170817, *Eur. Phys. J. A* **55**, 80 (2019).
- [17] B. Margalit and B. D. Metzger, Constraining the maximum mass of neutron stars from multi-messenger ob-

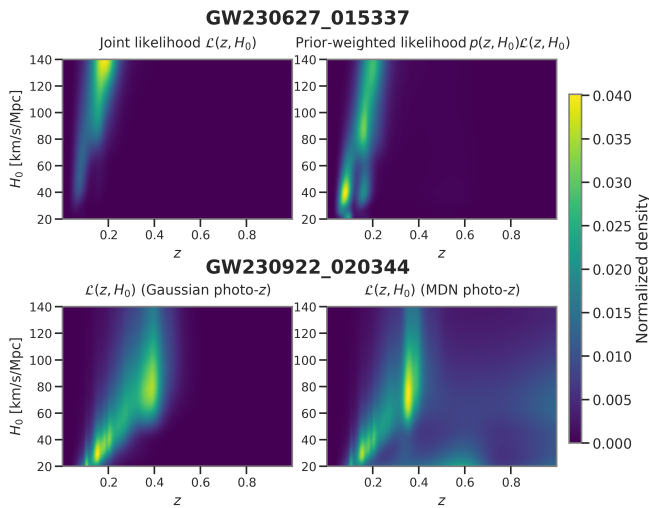


FIG. 9. Two-dimensional joint GW-EM likelihood in the (z, H_0) plane for GW230627_015337 (top row) and GW230922_020344 (bottom row). In the top row, the left panel shows the joint likelihood $\mathcal{L}(z, H_0)$, while the right panel shows the integrand of the marginalized likelihood obtained when adopting a redshift prior uniform in comoving volume ($p(z, H_0) \propto dV/dz$). The bottom row displays the likelihood for GW230922_020344 computed using two different photo- z PDF treatments: a Gaussian approximation (left) and the full photo- z PDF predicted by the MDN (right). Colors represent the normalized probability density.

servations of gw170817, *ApJL* **850**, L19 (2017).

- [18] D. Radice and L. Dai, Multimessenger parameter estimation of gw170817, *Eur. Phys. J. A* **55**, 50 (2019).
- [19] P. S. Cowperthwaite, E. Berger, V. A. Villar, and et al., The electromagnetic counterpart of the binary neutron star merger ligo/virgo gw170817. ii. uv, optical, and near-infrared light curves and comparison to kilonova models, *ApJL* **848**, L17 (2017).
- [20] M. M. Kasliwal, E. Nakar, L. P. Singer, and et al., Illuminating gravitational waves: A concordant picture of photons from a neutron star merge, *Science* **6370**, 1559 (2017).
- [21] E. Waxman, E. O. Ofek, D. Kushnir, and A. Gal-Yam, Constraints on the ejecta of the gw170817 neutron star merger from its electromagnetic emission, *MNRAS* **481**, 3423–3441 (2018).
- [22] L. Verde, T. Treu, and A. G. Riess, Tensions between the early and late Universe, *Nat. Astron.* **3**, 891 (2019), [arXiv:1907.10625 \[astro-ph.CO\]](https://arxiv.org/abs/1907.10625).
- [23] E. Di Valentino, O. Mena, S. Pan, and et al., In the realm of the hubble tension—a review of solutions, *Class. Quantum Grav.* **38**, 153001 (2021).
- [24] E. Abdalla, G. F. Abellán, A. Aboubrahim, and et al., Cosmology intertwined: A review of the particle physics, astrophysics, and cosmology associated with the cosmological tensions and anomalies, *JHEAP* **34**, 49 (2022).
- [25] Planck Collaboration, N. Aghanim, Y. Akrami, M. Ashdown, and et al., Planck 2018 results. VI. Cosmological parameters, *A&A* **641**, 67 (2020).
- [26] L. Breuval, A. G. Riess, S. Casertano, and et al., Small magellanic cloud cepheids observed with the hubble space telescope provide a new anchor for the sh0es distance ladder, *ApJ* **973**, 30 (2024).
- [27] T. Hamana, M. Shirasaki, S. Miyazaki, and et al., Cosmological constraints from cosmic shear two-point correlation functions with hsc survey first-year data, *PASJ* **72**, 16 (2020).
- [28] M. Asgari, C.-H. Lin, B. Joachimi, and et al., Kids-1000 cosmology: Cosmic shear constraints and comparison between two point statistics, *A&A* **645**, A104 (2021).
- [29] R. Dalal, X. Li, A. Nicola, and et al., Hyper supprimecam year 3 results: Cosmology from cosmic shear power spectra, *Phys. Rev. D* **108**, 123519 (2023).
- [30] A. Amon, D. Gruen, M. A. Troxel, and et al., Dark energy survey year 3 results: Cosmology from cosmic shear and robustness to data calibration, *Phys. Rev. D* **105**, 023514 (2024).
- [31] K. Lodha, R. Calderon, W. L. Matthewson, and et al., Extended dark energy analysis using desi dr2 bao measurements, *Phys. Rev. D* **112**, 083511 (2025).
- [32] M. A. Karim, J. Aguilar, S. Ahlen, and et al., Desi dr2 results. ii. measurements of baryon acoustic oscillations and cosmological constraints, *Phys. Rev. D* **112**, 083515 (2025).
- [33] B. F. Schutz, Determining the Hubble constant from gravitational wave observations, *Nature* **323**, 310 (1986).
- [34] D. E. Holz and S. A. Hughes, Using Gravitational-Wave Standard Sirens, *ApJ* **629**, 15 (2005).
- [35] N. Dalal, D. E. Holz, S. A. Hughes, and B. Jain, Short grb and binary black hole standard sirens as a probe of dark energy, *Phys. Rev. D* **74**, 063006 (2006).
- [36] B. P. Abbott, R. Abbott, T. D. Abbott, F. Acernese, K. Ackley, and et al. (LIGO Scientific Collaboration and Virgo Collaboration), Gw170817: Observation of gravitational waves from a binary neutron star inspiral, *Phys. Rev. Lett.* **119**, 161101 (2017).
- [37] B. P. Abbott, R. Abbott, T. D. Abbott, F. Acernese, K. Ackley, C. Adams, T. Adams, P. Addesso, R. X. Adhikari, V. B. Adya, and et al., A gravitational-wave standard siren measurement of the Hubble constant, *Nature* **551**, 85 (2017).
- [38] D. A. Coulter, R. J. Foley, C. D. Kilpatrick, and et al., Swope supernova survey 2017a (sss17a), the optical counterpart to a gravitational wave source, *Science* **358**, 1556 (2017).
- [39] M. Soares-Santos, D. E. Holz, J. Annis, and et al., The Electromagnetic Counterpart of the Binary Neutron Star Merger LIGO/Virgo GW170817. I. Discovery of the Optical Counterpart Using the Dark Energy Camera, *ApJL* **848**, L16 (2017).
- [40] S. Valenti, David, J. Sand, S. Yang, and et al., The Discovery of the Electromagnetic Counterpart of GW170817: Kilonova AT 2017gfo/DLT17ck, *ApJL* **848**, L24 (2017).
- [41] I. Arcavi, G. Hosseinzadeh, D. A. Howell, and et al., Optical emission from a kilonova following a gravitational-wave-detected neutron-star merger, *Nature* **551**, 64 (2017).
- [42] N. R. Tanvir, A. J. Levan, C. González-Fernández, and et al., The Emergence of a Lanthanide-rich Kilonova Following the Merger of Two Neutron Stars, *ApJL* **848**, L27 (2017).
- [43] V. M. Lipunov, E. Gorbovskoy, V. G. Kornilov,

- and et al., MASTER Optical Detection of the First LIGO/Virgo Neutron Star Binary Merger GW170817, *ApJL* **850**, L1 (2017).
- [44] W. Del Pozzo, Inference of cosmological parameters from gravitational waves: Applications to second generation interferometers, *Phys. Rev. D* **86**, 043011 (2012), [arXiv:1108.1317](#).
- [45] M. Soares-Santos, A. Palmese, W. Hartley, and et al., First Measurement of the Hubble Constant from a Dark Standard Siren using the Dark Energy Survey Galaxies and the LIGO/Virgo Binary-Black-hole Merger GW170814, *ApJL* **876**, L7 (2019).
- [46] M. Fishbach, R. Gray, I. Magaña Hernandez, and et al., A Standard Siren Measurement of the Hubble Constant from GW170817 without the Electromagnetic Counterpart, *ApJL* **871**, L13 (2019).
- [47] A. Palmese, C. R. Bom, S. Mucesh, and W. G. Hartley, A standard siren measurement of the hubble constant using gravitational-wave events from the first three ligo/virgo observing runs and the desi legacy survey, *ApJ* **943**, 56 (2023).
- [48] R. Gray, F. Beirnaert, C. Karathanasis, and et al., Joint cosmological and gravitational-wave population inference using dark sirens and galaxy catalogues, *JCAP* **108**, 042002.
- [49] S. Mastroianni, D. Laghi, R. Gray, and et al., Joint population and cosmological properties inference with gravitational waves standard sirens and galaxy surveys, *Phys. Rev. D* **108**, 042002 (2023).
- [50] V. Alfradique, C. R. Bom, and A. e. a. Palmese, A dark siren measurement of the Hubble constant using gravitational wave events from the first three LIGO/Virgo observing runs and DELVE, *MNRAS* **528**, 3249–3259 (2024).
- [51] C. R. Bom, V. Alfradique, A. Palmese, G. Teixeira, and et al., A dark standard siren measurement of the Hubble constant following LIGO/Virgo/KAGRA O4a and previous runs, *MNRAS* **535**, 961–975 (2024).
- [52] A. G. Abac and et al. (LIGO Scientific Collaboration, Virgo Collaboration, and KAGRA Collaboration), Gwtc-4.0: Constraints on the cosmic expansion rate and modified gravitational-wave propagation, arXiv e-prints [arXiv:2509.04348](#), [arXiv:2509.04348](#) (2025), [arXiv:2509.04348 \[astro-ph.GA\]](#).
- [53] G. Pierra and A. Papadopoulos, Heavy black-holes also matter in standard siren cosmology, arXiv e-prints [arXiv:2601.03257](#), [arXiv:2601.03257](#) (2026), [arXiv:2601.03257 \[astro-ph.GA\]](#).
- [54] I. McMahon, D. Laghi, M. Soares-Santos, and et al., Measurement of the Hubble constant using the Dark Energy Survey Year 6 Gold galaxy catalog and the fourth Gravitational-Wave Transient Catalog, arXiv e-prints [arXiv:2602.04766](#), [arXiv:2602.04766](#) (2026), [arXiv:2602.04766 \[astro-ph.GA\]](#).
- [55] T. Namikawa, A. Nishizawa, and A. Taruya, Anisotropies of gravitational-wave standard sirens as a new cosmological probe without redshift information, *Phys. Rev. Lett.* **116**, 121302 (2016).
- [56] S. Mukherjee, B. D. Wandelt, S. M. , B. D. Nissanke, and A. Silvestri, Accurate precision cosmology with redshift unknown gravitational wave sources, *Phys. Rev. D* **103**, 043520 (2021).
- [57] S. Mukherjee, B. D. Wandelt, and J. Silk, Testing the general theory of relativity using gravitational wave propagation from dark standard sirens, *MNRAS* **502**, 1136–1144 (2021).
- [58] C. Cigarrán Díaz and S. Mukherjee, Mapping the cosmic expansion history from LIGO-Virgo-KAGRA in synergy with DESI and SPHEREx, *Mon. Not. R. Astron. Soc.* **511**, 2782 (2022).
- [59] S. Mukherjee, A. Krolewski, B. D. Wandelt, and J. Silk, Cross-correlating Dark Sirens and Galaxies: Constraints on H0 from GWTC-3 of LIGO–Virgo–KAGRA, *ApJ* **975**, 189 (2024).
- [60] T. Ghosh, S. More, S. Bera, and S. Bose, Bayesian framework to infer the hubble constant from the cross-correlation of individual gravitational wave events with galaxies, *Phys. Rev. D* **111**, 063513 (2025).
- [61] I. S. de Matos, C. Dalang, T. Baker, and et al., First measurement of the Hubble constant from gravitational wave-galaxy cross-correlations, arXiv e-prints [arXiv:2512.15380](#), [arXiv:2512.15380](#) (2025), [arXiv:2512.15380 \[astro-ph.GA\]](#).
- [62] J. Ezquiaga, Hearing gravity from the cosmos: GWTC-2 probes general relativity at cosmological scales, *Phys. Lett. B* **822**, 136665 (2021).
- [63] J. Ezquiaga and D. Holz, Spectral Sirens: Cosmology from the Full Mass Distribution of Compact Binaries, *Phys. Rev. Lett.* **129**, 061102 (2022).
- [64] N. Borghi, M. Mancarella, M. Moresco, and et al., Cosmology and astrophysics with standard sirens and galaxy catalogs in view of future gravitational wave observations, *ApJ* **964**, 191 (2024).
- [65] I. Magaña Hernandez and A. Palmese, Spectral siren cosmology from gravitational-wave observations in GWTC-4.0, arXiv e-prints [arXiv:2509.03607](#), [arXiv:2509.03607](#) (2025), [arXiv:2509.03607 \[astro-ph.GA\]](#).
- [66] A. Farah, T. Callister, J. Ezquiaga, and et al., No need to know: astrophysics-free gravitational-wave cosmology, *ApJ* **978**, 153 (2025).
- [67] M. Tagliacruzchi, M. Moresco, N. Borghi, and M. Fiebig, Accelerating the standard siren method: Improved constraints on modified gravitational-wave propagation with future data, *A&A* **702**, 13 (2025).
- [68] M. Tagliacruzchi, M. Moresco, N. Borghi, and C. Ciapetti, Mind the peak: improving cosmological constraints from gwtc-4.0 spectral sirens using semiparametric mass models, arXiv e-prints [arXiv:2601.03347](#), [arXiv:2601.03347](#) (2026), [arXiv:2601.03347 \[astro-ph.GA\]](#).
- [69] H. Tong, M. Fishbach, and E. Thrane, Spinning spectral sirens: Robust cosmological measurement using mass–spin correlations in the binary black hole population, *ApJ* **985**, 220 (2025).
- [70] D. Chatterjee, A. Hegade K. R., G. Holder, and et al., Cosmology with love: Measuring the hubble constant using neutron star universal relations, *Phys. Rev. D* **104**, 083528 (2021).
- [71] T. Ghosh, B. Biswas, and S. Bose, Simultaneous inference of neutron star equation of state and the hubble constant with a population of merging neutron stars, *Phys. Rev. D* **106**, 123529 (2022).
- [72] A. G. Abac and et al. (LIGO Scientific Collaboration, Virgo Collaboration, and KAGRA Collaboration), Gwtc-4.0: Updating the gravitational-wave transient catalog with observations from the first part of the fourth ligo-virgo-kagra observing run, arXiv

- e-prints [arXiv:2508.18082](https://arxiv.org/abs/2508.18082), [arXiv:2508.18082](https://arxiv.org/abs/2508.18082) (2025), [arXiv:2508.18082](https://arxiv.org/abs/2508.18082) [[astro-ph.GA](https://arxiv.org/abs/2508.18082)].
- [73] . K. C. LIGO Scientific Collaboration, Virgo Collaboration, Gwtc-4.0: Parameter estimation data release [data set], Zenodo [10.5281/zenodo.17014085](https://zenodo.org/record/17014085) (2025).
- [74] P. Fernique, T. Boch, and T. e. a. Donaldson, MOC - HEALPix Multi-Order Coverage map Version 1.0, arXiv e-prints [arXiv:1505.02937](https://arxiv.org/abs/1505.02937), [arXiv:1505.02937](https://arxiv.org/abs/1505.02937) (2014), [arXiv:1505.02937](https://arxiv.org/abs/1505.02937) [[astro-ph.IM](https://arxiv.org/abs/1505.02937)].
- [75] K. M. Górski, E. Hivon, A. J. Banday, and et al., HEALPix: A Framework for High-Resolution Discretization and Fast Analysis of Data Distributed on the Sphere, *ApJ* **622**, 759 (2005).
- [76] Planck Collaboration, Ade, P. A. R., Aghanim, N., Arnaud, M., and et al., Planck 2015 results - xiii. cosmological parameters, *A&A* **594**, A13 (2016).
- [77] H.-Y. Chen, M. Fishbach, and D. E. Holz, A two per cent Hubble constant measurement from standard sirens within five years, *Nature* **562**, 545 (2018).
- [78] A. Finke, S. Foffa, F. Iacovelli, and et al., Cosmology with ligo/virgo dark sirens: Hubble parameter and modified gravitational wave propagation, *JCAP* **08**, 026.
- [79] R. Gray, C. Messenger, and J. Veitch, A pixelated approach to galaxy catalogue incompleteness: improving the dark siren measurement of the hubble constant, *MNRAS* **512**, 1127–1140 (2022).
- [80] A. Dey, D. J. Schlegel, D. Lang, and et al., Overview of the DESI Legacy Imaging Surveys, *AJ* **157**, 168 (2019).
- [81] R. D. Blum, K. Burleigh, A. Dey, and et al., The DECam Legacy Survey, in *American Astronomical Society Meeting Abstracts #228*, American Astronomical Society Meeting Abstracts, Vol. 228 (2016) p. 317.01.
- [82] H. Zou, X. Zhou, X. Fan, and et al., Project Overview of the Beijing–Arizona Sky Survey, *PASP* **129**, 064101 (2017).
- [83] D. R. Silva, R. D. Blum, L. Allen, et al., The Mayall z-band Legacy Survey, in *American Astronomical Society Meeting Abstracts*, Bulletin of the American Astronomical Society, Vol. 228 (2016) p. 317.02, aAS Meeting Abstract #228.
- [84] B. Flaugher, H. T. Diehl, K. Honscheid, and et al., The dark energy camera, *AJ* **150**, 150 (2015).
- [85] T. M. C. Abbott, M. Adamów, M. Aguena, and et al., The Dark Energy Survey Data Release 2, *ApJS* **255**, 20 (2021).
- [86] A. Drlica-Wagner, P. S. Ferguson, M. Adamów, and et al., The DECam Local Volume Exploration Survey Data Release 2, *ApJS* **261**, 38 (2022).
- [87] <https://noirlab.edu/science/programs/ctio/instruments/Dark-Energy-Camera/DeROSITAS>.
- [88] Data are available at <https://www.legacysurvey.org/dr10>.
- [89] Data are available at <https://www.legacysurvey.org/dr9>.
- [90] M. R. Blanton, D. W. Hogg, N. A. Bahcall, and et al., The galaxy luminosity function and luminosity density at redshift $z = 0.11$, *ApJ* **592**, 819–838 (2003).
- [91] A. Palmese, J. deVicente, M. E. S. Pereira, and et al., A Statistical Standard Siren Measurement of the Hubble Constant from the LIGO/Virgo Gravitational Wave Compact Object Merger GW190814 and Dark Energy Survey Galaxies, *ApJL* **900**, L33 (2020).
- [92] C. Bishop, Mixture density networks, *Aston University*, 26 (1994).
- [93] G. Teixeira, C. Bom, L. Santana-Silva, and et al., Photometric redshifts probability density estimation from recurrent neural networks in the decam local volume exploration survey data release 2, *Astron. Comput.* **49**, 100886 (2024).
- [94] G. Teixeira and et al., Photometric redshifts for the desi legacy imaging survey using deep learning probability density estimators (in preparation), in preparation.
- [95] M. C. Artale, M. Mapelli, N. Giacobbo, and et al., Host galaxies of merging compact objects: mass, star formation rate, metallicity, and colours, *MNRAS* **487**, 1675–1688 (2019).
- [96] M. C. Artale, M. Mapelli, Y. Bouffanais, and et al., Mass and star formation rate of the host galaxies of compact binary mergers across cosmic time, *MNRAS* **491**, 3419–3434 (2019).
- [97] F. Santoliquido, M. Mapelli, M. C. Artale, and et al., Modelling the host galaxies of binary compact object mergers with observational scaling relations, *MNRAS* **516**, 3297–3317 (2022).
- [98] L. Rauf, C. Howlett, T. M. Davis, and et al., Exploring binary black hole mergers and host galaxies with shark and compas, *MNRAS* **523**, 5719–5737 (2024).
- [99] M. Pálfi, G. Dálya, and P. Raffai, Utilizing stellar mass estimates to identify gravitational wave host galaxies, *MNRAS* **539**, 1879–1893 (2025).
- [100] M. Madau, Piero & Dickinson, Cosmic star-formation history, *Annu. Rev. Astron. Astrophys.* **52**, 71 (2014).
- [101] C. S. Kochanek, M. A. Pahre, E. E. Falco, and et al., The k-band galaxy luminosity function, *ApJ* **560**, 566 (2001).
- [102] L. P. Singer, H.-Y. Chen, D. E. Holz, and et al., Supplement: Going the distance: Mapping host galaxies of ligo and virgo sources in three dimensions using local cosmography and targeted follow-up, *ApJS* **226**, 10 (2016).
- [103] W. Fong, E. Berger, R. Chornock, and et al., Demographics of the galaxies hosting short-duration gamma-ray bursts, *ApJ* **769**, 56 (2013).
- [104] C. N. Leibler and E. Berger, The stellar ages and masses of short gamma-ray burst host galaxies: Investigating the progenitor delay time distribution and the role of mass and star formation in the short gamma-ray burst rate, *ApJ* **725**, 1202 (2010).
- [105] L. P. Singer and L. R. Price, Rapid bayesian position reconstruction for gravitational-wave transients, *Phys. Rev. D* **93**, 024013 (2016).
- [106] T. A. Callister and W. M. Farr, Parameter-free tour of the binary black hole population, *Phys. Rev. X* **14**, 021005 (2024).
- [107] A. G. Abac and et al. (LIGO Scientific Collaboration, Virgo Collaboration, and KAGRA Collaboration), Gwtc-4.0: Population properties of merging compact binaries, arXiv e-prints [arXiv:2508.18083](https://arxiv.org/abs/2508.18083), [arXiv:2508.18083](https://arxiv.org/abs/2508.18083) (2025), [arXiv:2508.18083](https://arxiv.org/abs/2508.18083) [[astro-ph.GA](https://arxiv.org/abs/2508.18083)].
- [108] I. Mandel, W. M. Farr, and J. R. Gair, Extracting distribution parameters from multiple uncertain observations with selection biases, *MNRAS* **486**, 1086 (2019).
- [109] R. Gray, I. Magaña Hernandez, H. Qi, and et al., Cosmological inference using gravitational wave standard sirens: A mock data analysis, *Phys. Rev. D* **101**, 122001 (2020).

- [110] L. P. Singer, H.-Y. Chen, D. E. Holz, and et al., Going the distance: Mapping host galaxies of ligo and virgo sources in three dimensions using local cosmography and targeted follow-up, *ApJ* **829**, L15 (2016).
- [111] . K. C. LIGO Scientific Collaboration, Virgo Collaboration, Gwtc-4.0: O4a search sensitivity estimates [data set], Zenodo [10.5281/zenodo.16740117](https://zenodo.org/record/16740117) (2025).
- [112] R. Essick, M. W. Coughlin, M. Zevin, and et al. (LIGO Scientific Collaboration, Virgo Collaboration, and KAGRA Collaboration), Compact binary coalescence sensitivity estimates with injection campaigns during the ligo-virgo-kagra collaborations' fourth observing run, *Phys. Rev. D* **112**, 102001 (2025).
- [113] H.-Y. Chen, Systematic uncertainty of standard sirens from the viewing angle of binary neutron star inspirals, *Phys. Rev. Lett.* **125**, 201301 (2020).
- [114] M. Mancarella, F. Iacovelli, S. Foffa, and et al., Accurate standard siren cosmology with joint gravitational-wave and γ -ray burst observations, *Phys. Rev. Lett.* **133**, 261001 (2020).
- [115] A. Salvarese and H.-Y. Chen, Mitigating the binary viewing angle bias for standard sirens, *ApJL* **974**, L16 (2024).
- [116] M. Müller, S. Mukherjee, and G. Ryan, Be careful in multimessenger inference of the hubble constant: A path forward for robust inference, *ApJL* **977**, L45 (2024).
- [117] H.-Y. Chen, C. Talbot, and E. A. Chase, Mitigating the counterpart selection effect for standard sirens, *Phys. Rev. Lett.* **974**, L16 (2024).
- [118] V. Alfradique, C. R. Bom, and T. Castro, Systematic bias in dark siren statistical methods and its impact on hubble constant measurement, *Phys. Rev. D* **112**, 063561 (2025).
- [119] B. P. Abbott, R. Abbott, T. D. Abbott, and et al., A gravitational-wave measurement of the hubble constant following the second observing run of advanced ligo and virgo, *ApJ* **909**, 218 (2021).
- [120] R. Abbott, H. Abe, F. Acernese, and et al., Constraints on the cosmic expansion history from gwtc-3, *Astrophys. J.* **949**, 37 (2023).
- [121] K. Leyde, T. Baker, and W. Enzi, Cosmic cartography ii: completing galaxy catalogs for gravitational-wave cosmology, arXiv e-prints [arXiv:2507.12171](https://arxiv.org/abs/2507.12171), arXiv:2507.12171 (2025), [arXiv:2507.12171](https://arxiv.org/abs/2507.12171) [astro-ph.GA].
- [122] C. Talbot and E. Thrane, Measuring the binary black hole mass spectrum with an astrophysically motivated parameterization, *Astrophys. J.* **856**, 173 (2018).
- [123] M. Fishbach, D. E. Holz, and W. M. Farr, Does the black hole merger rate evolve with redshift?, *ApJL* **863**, L41 (2018).
- [124] B. Edelman, Z. Doctor, J. Godfrey, and B. Farr, Ain't no mountain high enough: Semiparametric modeling of ligo-virgo's binary black hole mass distribution, *ApJ* **924**, 101 (2022).
- [125] B. Edelman, B. Farr, and Z. Doctor, Cover your basis: Comprehensive data-driven characterization of the binary black hole population, *ApJ* **946**, 16 (2023).
- [126] C. Nicolaou, O. Lahav, P. Lemos, W. Hartley, and J. Braden, The impact of peculiar velocities on the estimation of the hubble constant from gravitational wave standard sirens, *MNRAS* **495**, 90 (2020).
- [127] S. Mukherjee, G. Lavaux, F. R. Bouchet, J. Jasche, B. D. Wandelt, S. Nissanke, F. Leclercq, and K. Hotokezaka, Velocity correction for hubble constant measurements from standard sirens, *A&A* **646**, 11 (2021).
- [128] The KL divergence [? ?] between two probability densities $p(x)$ and $q(x)$ is defined as $D_{\text{KL}}(P||Q) = \int p(x) \log[p(x)/q(x)] dx$.
- [129] G. Dálya, R. Díaz, F. R. Bouchet, Z. Frei, J. Jasche, G. Lavaux, R. Macas, S. Mukherjee, M. Pálfi, R. S. de Souza, B. D. Wandelt, M. Bilicki, and P. Raffai, GLADE+: An Extended Galaxy Catalogue for Multimessenger Searches with Advanced Gravitational-wave Detectors, *MNRAS* **514**, 1403–1411 (2022).
- [130] A. G. Hanselman, A. Vijaykumar, M. Fishbach, and D. Holz, Gravitational-wave dark siren cosmology systematics from galaxy weighting, *ApJ* **979**, 9 (2025).
- [131] N. Borghi, M. Moresco, M. Tagliacucci, and G. Cuomo, Echoes from the dark: Galaxy catalog incompleteness in standard siren cosmology, *A&A* **706**, 14 (2026).
- [132] G. Perna, S. Mastroianni, and A. Ricciardone, Investigating the impact of galaxies' compact binary hosting probability for gravitational-wave cosmology, *A&A* **698**, A128 (2025).
- [133] F. Santoliquido, M. Mapelli, N. Giacobbo, and et al., The cosmic merger rate density of compact objects: impact of star formation, metallicity, initial mass function, and binary evolution, *MNRAS* **502**, 4877 (2021).
- [134] S. Mandhai, G. P. Lamb, N. R. Tanvir, and et al., Exploring compact binary merger host galaxies and environments with zelda, *MNRAS* **514**, 2716 (2022).
- [135] Z. Ivezić, S. M. Kahn, J. A. Tyson, and et al., Lsst: From science drivers to reference design and anticipated data products, *ApJ* **873**, 111 (2019).
- [136] C. Turcki, M. Bilicki, G. Dálya, and et al., Impact of modelling galaxy redshift uncertainties on the gravitational-wave dark standard siren measurement of the Hubble constant, *MNRAS* **526**, 6224–6233 (2023).
- [137] H. Oyaizu, M. Lima, C. E. Cunha, and et al, Photometric Redshift Error Estimators, *ApJ* **689**, 689 (2008).
- [138] C. Bonnett, M. A. Troxel, W. Hartley, and et al. (Dark Energy Survey Collaboration), Redshift distributions of galaxies in the dark energy survey science verification shear catalogue and implications for weak lensing, *Phys. Rev. D* **94**, 042005 (2016).
- [139] M. Tanaka, J. Coupon, B.-C. Hsieh, and et al., Photometric redshifts for hyper supprime-cam subaru strategic program data release 1, *PASJ* **70**, S9 (2017).